

AD 623096

**Measurement of Fluid Properties for
Magnetoplasmadynamic Power Generators**

Ninth Quarterly Technical Summary Report

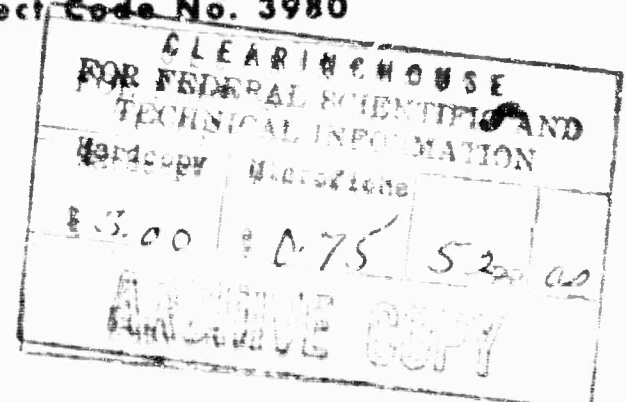
(1 May—31 August 1965)

Contract No. Nonr-4104(j) and Amendment 1

Order No.: ARPA 420

Project Code No. 3980

EDR 4400



DDC

Allison Division • General Motors

Indianapolis, Indiana

**BEST
AVAILABLE COPY**

**MISSING PAGE
NUMBERS ARE BLANK
AND WERE NOT
FILMED**

**Measurement of Fluid Properties for
Magnetoplasmadynamic Power Generators**
Ninth Quarterly Technical Summary Report
(1 May—31 August 1965)

Contract No. Nonr-4104(00) and Amendment 1
Order No.: ARPA 420 Project Code No. 3980

EDR 4400

13 September 1965

R.T. Schneider

R. T. Schneider,
Program Manager

F. G. Myers

F. G. Myers
Research Director

Allison

FOREWORD

This technical summary report was prepared by the Research Department of Allison Division of General Motors. It describes the work accomplished under Contract Nonr-4104(00) for the period 1 May—31 August 1965.

The program was sponsored by the Office of Naval Research under the direction of Mr. J. A. Satkowski.

The report was written by Dr. Richard T. Schneider and Dr. Horst E. Wilhelm. Other members of the Allison Research team who contributed to the work were R. L. Koch, D. L. Clingman, R. O. Whitaker, R. L. Holtman, and J. A. Eriksen, Jr.

Heater design and fabrication supervision was provided by Prof. W. Kluge and Dr. W. Bloss of the Technical University, Stuttgart, Germany, consultants to Allison Division of General Motors.

Allison

TABLE OF CONTENTS

<u>Section</u>	<u>Title</u>	<u>Page</u>
I	Introduction	1
II	Generator Design	3
	Duct	3
	Heater	6
III	MPD Generator Checkout Runs	15
IV	Helium-Cesium Runs	19
V	Discussion of Results	27
VI	Nonequilibrium Processes in Magnetoactive Plasma Flows	31
	Field Equations	31
	Plasma Flow Model	35
	Numerical Results and Analytical Discussions	37
	Change of Mean Flow Fields	37
	Buildup of Nonequilibrium Electron Temperature	40
	Buildup of Nonequilibrium Electron Intensity	43
	Conclusions	46
VII	Conclusions	49
VIII	References	51

Allison

LIST OF ILLUSTRATIONS

<u>Figure</u>	<u>Title</u>	<u>Page</u>
1	Cross section of the MPD generator test section	4
2	Ceramic parts for cavity design.	5
3	Side view of the MPD test section	7
4	Generator duct with magnet pole pieces attached	9
5	Schematic of the heater	11
6	Assembled MPD power generator	13
7	Open circuit voltage vs magnetic field—seeding > 2%	19
8	Reduced seeding ratio and 100 kilohm leakage resistance	20
9	Curve showing pronounced decrease in open circuit voltage above 2 Tesla	21
10	Output voltage for various electrode lengths	21
11	Saturation overcome by increasing the seeding ratio	22
12	Typical I-V curves in saturated mode	23
13	8-channel strip chart data recording	24
14	Comparison of theoretical and observed curves of output vs electrode numbers	25
15	8-channel measurement of Hall voltages	26
16	Velocity and emf profile across channel	27
17	Schematic for internal shorting—open circuit	28
18	Schematic for internal shorting with load applied.	29
19	Geometry of flow fields	36
20	Mean flow fields	39
21	Intercomponent thermal nonequilibrium.	42
22	Buildup of electron density.	45
23	Buildup of current density	47

Allison

LIST OF TABLES

<u>Table</u>	<u>Title</u>	<u>Page</u>
I	MPD power generator design data	10
II	Initial flow values	36
III	Elementary particle constants	37
IV	Plateau electron temperatures.	43
V	Relaxation lengths	44

Allison

I. INTRODUCTION

This report describes the progress on Contract Nonr-104(00) for the period 1 May-31 August 1965. Design and operation of a relatively large, closed-loop MPD power generation research device are discussed.

The objective of the effort during the report period was to collect information which would permit determining the feasibility of closed-loop MPD power generation at low temperatures—i.e., 1500°K. It was felt that it would be necessary to employ a true closed-loop device rather than a blowdown device since the blowdown device avoids many of the difficulties necessary for study and gives data of a different type. The data which would be obtained by the blowdown device would require too much extrapolation. Also, with the blowdown device the observation time is short and the electrodes are cold rather than at operational temperature.

The difficulties encountered as a result of (1) investigations described herein, (2) previous investigations,^{1*} (3) investigations employing a smaller closed-loop device, and (4) investigations using three other existing true closed-loop devices^{2,3,4} were of a nature which could not be detected in a blowdown device.

The main difficulties encountered in the closed-loop device are summarized as follows:

- Corrosion of the components caused by cesium and by traces of oxygen and nitrogen
- Obtaining a smooth, steady injection of helium over extended time periods
- Separation of helium-cesium
- Partial or complete electrical shorting, caused by conducting deposits, between electrodes and between electrodes and ground
- Design of a reliable heater capable of heating a large mass flow of helium without introducing impurities

Some of these difficulties have been overcome and some need further work, as discussed in detail herein.

*Superscripts refer to references in Section VIII.

II. GENERATOR DESIGN

DUCT

Figure 1 shows a cross section of the new MPD generator test section. The walls of the duct (center portion of Figure 1) are formed by two layers of ceramic backed with a layer of tantalum. The layers of ceramic are kept from moving parallel to the tantalum wall by stainless steel brackets in the cold parts of the duct. Ceramic spacers are used to keep ceramic layers and the tantalum wall from moving toward each other. The two ceramic layers are kept in place by the shoulders on both sides of the ceramic spacers. These spacers form two cavities with ceramic shields between the cavities. Oversized holes in the shields prevent the ceramic material from touching the electrode stem before final contact is made in the colder portion of the duct where the electrode stem is held mechanically. Mechanical contact between the electrode and the ceramic is made by an electrode holder. The electrode holder is sufficiently removed from the hot zones of the duct to force leakage current in the ceramic to go through cold ceramic parts, where the electrical resistance is high.

With the cavity design as described, it was possible to overcome the electrode shorting problem caused by deposits of conducting material. The shield plate in front of the first cavity prevents most of the material from being deposited inside the first cavity. To short the electrode, the material being deposited must pass over two more shield plates and two more cavities—i.e., make a continuous plating—before an electrical contact is made. The photograph of the ceramic parts in Figure 2 illustrates more clearly how the cavity design works. Figure 2 also shows how the inner plates are held in place and how the outer plates are held apart.

The ceramic parts of the test section are made of alumina. In recent runs, however, the inner plates were made of boron nitride. The physical size of the channel shown in Figure 2 is as follows:

- Electrode distance—7 cm
- Channel width (between inner plates)—2 cm
- Total channel length (consisting of several elements as shown in Figure 2)—50 cm

A cooling channel is provided in the generator test section between the magnet pole pieces and the tantalum wall (re Figure 1). Cold helium gas is blown into this channel to protect the magnet pole pieces from heat. This gas is later mixed with the main gas stream. The magnet pole pieces, which are water cooled, form a part of the outer wall of the duct in such a way that they provide mechanical strength without having a sealing effect.

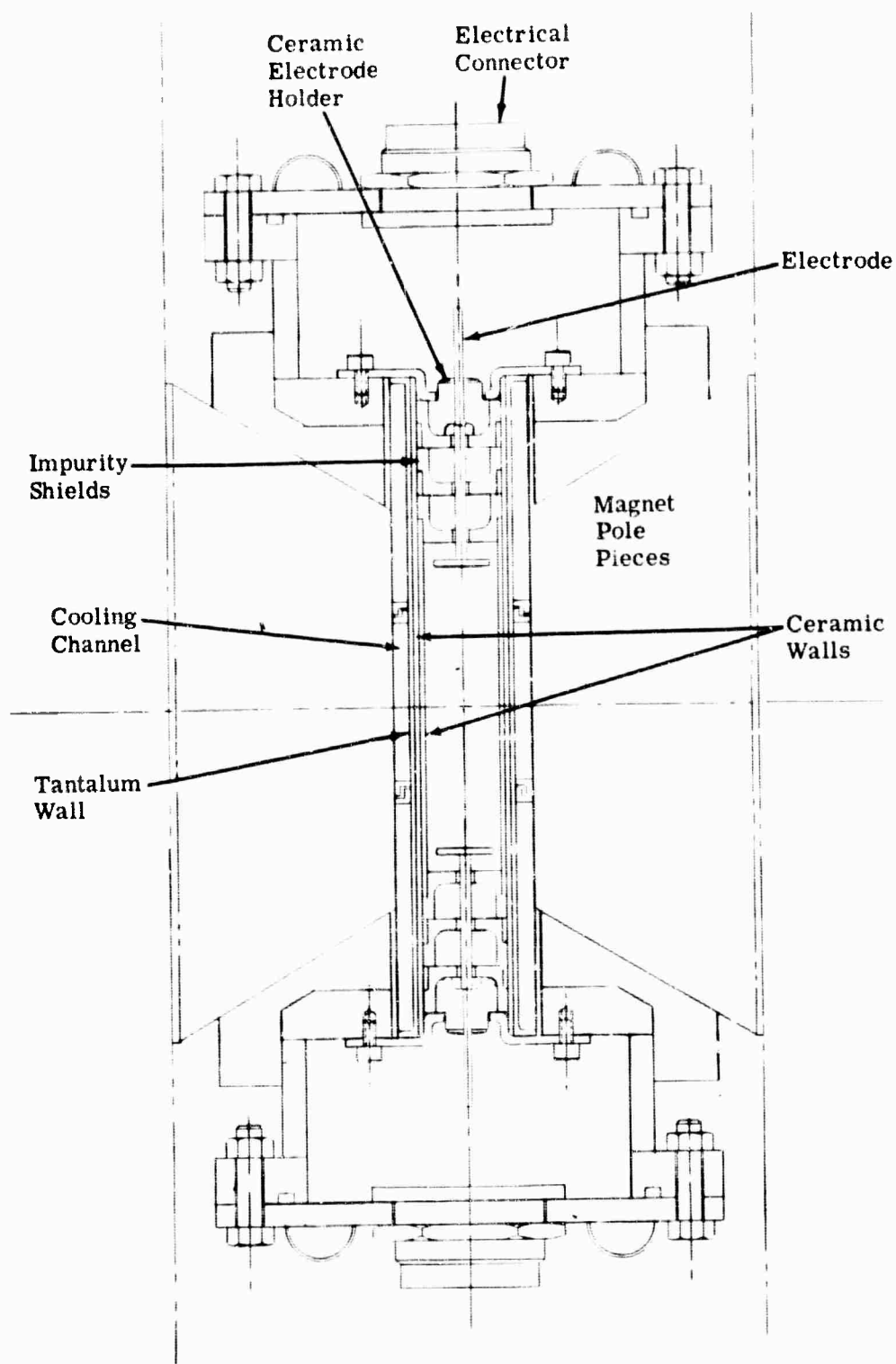


Figure 1. Cross section of the MPD generator test section (reference EX-71131).

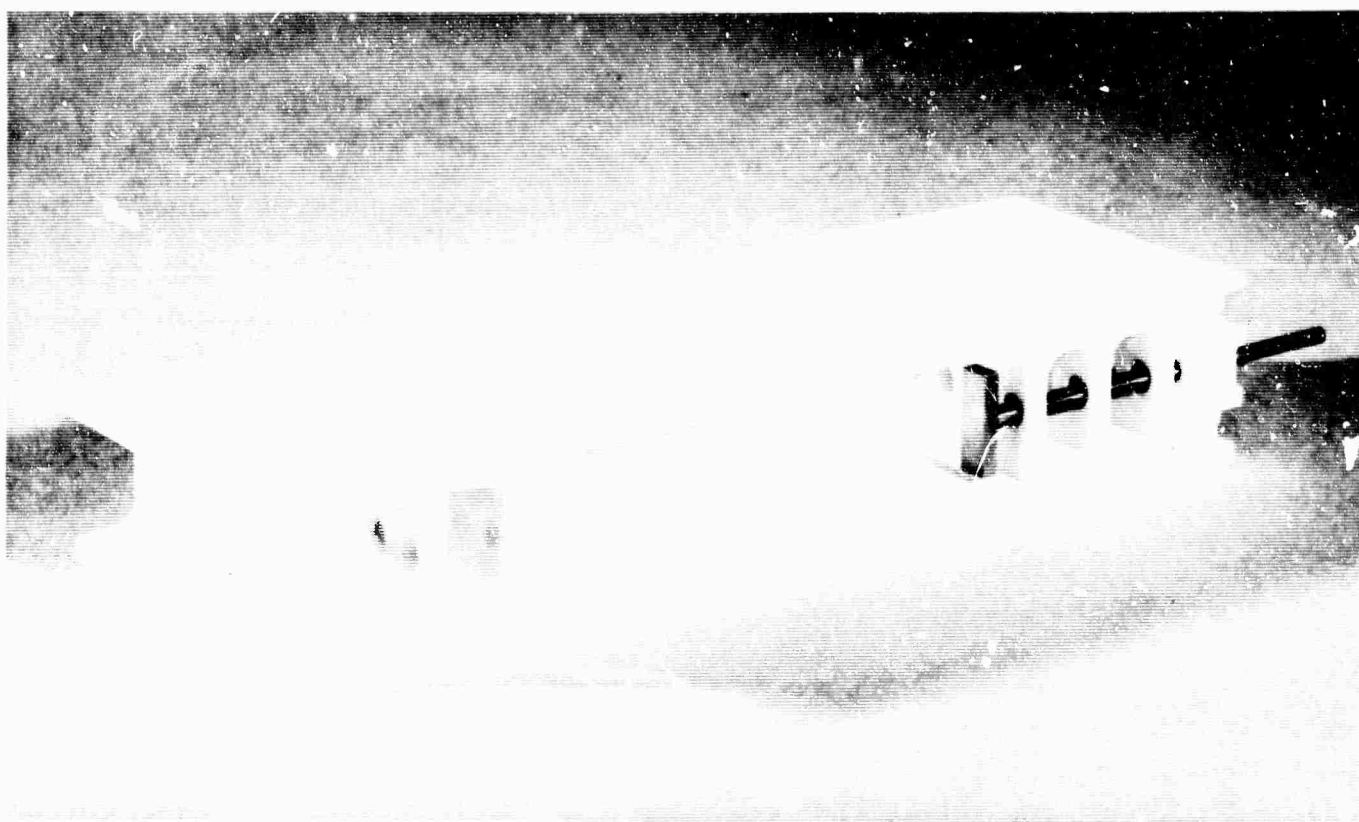


Figure 2. Ceramic parts for cavity design. Note manner of holding inner plates in place and outer plates apart.

The electrode distance can be varied by interchanging the inner ceramic plates of the duct. The height of these plates determines the electrode spacing.

Figure 3 shows the side view of the generator duct. A diagnostic box is attached to each end of the channel. Each box has a straight port for spectroscopic measurements and an inclined port for measurement of the electrode surface temperature. For additional observations, a pair of windows is mounted directly to the duct. Optical access was obtained by removing one electrode pair and using the stem holes as apertures. The number of electrode pairs, which varies between 57 and 67, depends on the electrode spacing used.

In the present buildup, different electrode materials are used alternately. These are pure tungsten, Philips Type A, and Philips Type B. The segmentation is as follows:

- Distance between center lines of neighboring electrodes—0.75 cm
- Electrode width—0.5 cm
- Free space between two neighboring electrodes—0.25 cm

Allison

The exit section of the duct is identical with the entrance—a diagnostic box is provided and may be used to obtain other diagnostic measurements.

Figure 4 is a photograph of the generator duct. The magnet pole pieces are attached. The observation windows are also visible.

HEATER

The experience gained from operation of the small heaters¹ was invaluable in designing the new heater, as described in the following paragraphs. First, it was impossible to support a heater element with an insulator when the heater was in the horizontal position—heater element temperature being necessarily too high for existing insulator materials to withstand. Consequently, the heater element was positioned vertically so that the insulator would be near the cooler portion only. (The heater element, when positioned vertically, does not require support in those areas which run hot.)

Secondly, it was necessary to design the heater element so that very little machining would be required in going from the raw material shape to the final shape. Each forming process invites cracks which ultimately cause failure during operation. Another requirement was that the heater element be designed to keep contamination, in form of metal vapor, in the gas to a minimum. As a final requirement, it was necessary that the heater be capable of shutdown from maximum to zero power within a few seconds.

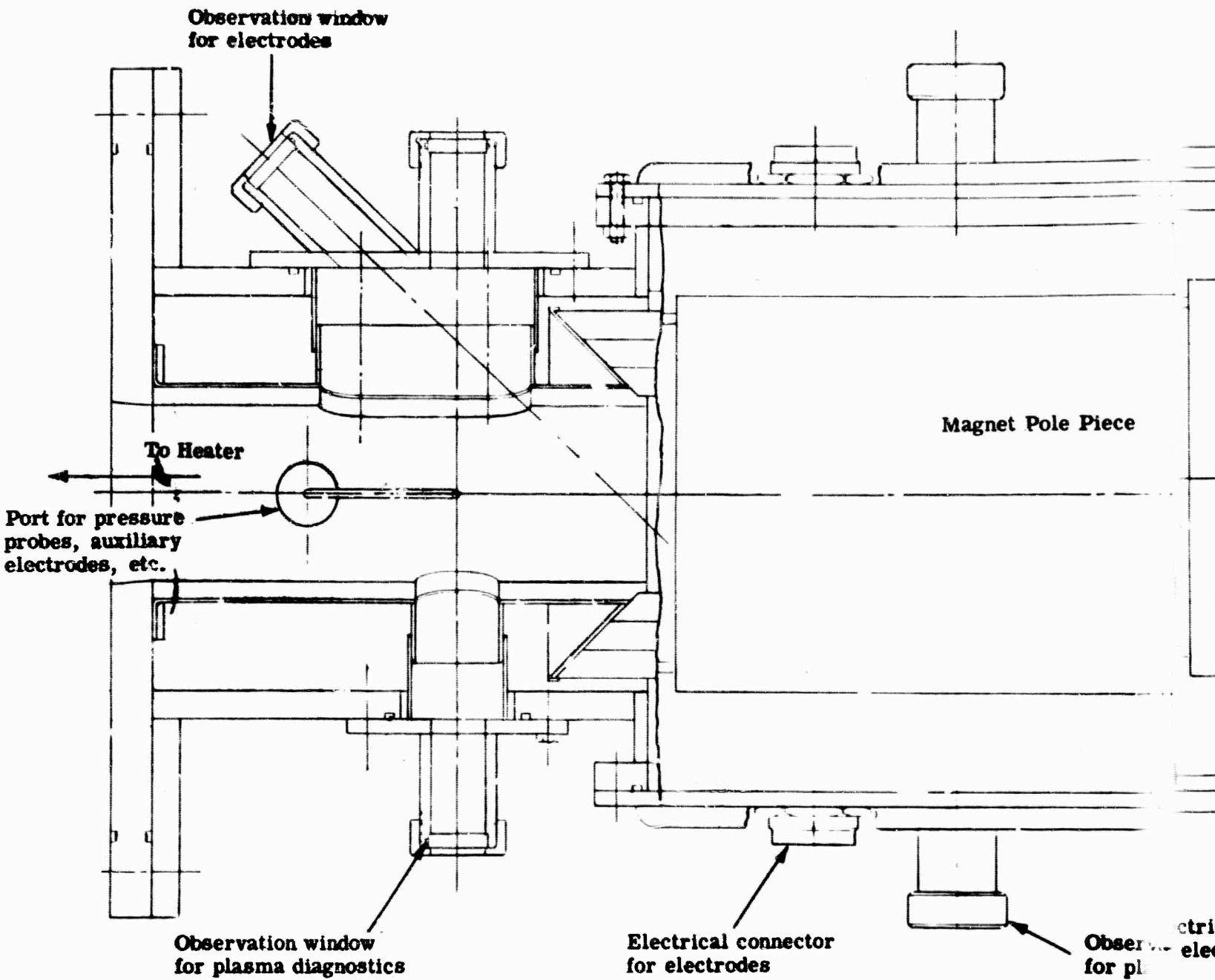
The final design of the heater which meets the requirements stated previously is shown in Figure 5. Since the heater was designed for vertical operation, the generator also operates in the vertical position.

As shown in Figure 5, helium enters through the helium inlet flange at room temperature. It flows through the tungsten radiation shields and cools them. On return through the heater, the helium is preheated as it passes along the tungsten box containing the heating elements. (The heating elements are not in direct contact with the working fluid.) After passing the tungsten box, the helium enters the main heater where it is brought up to 2000°K by radiation heating.

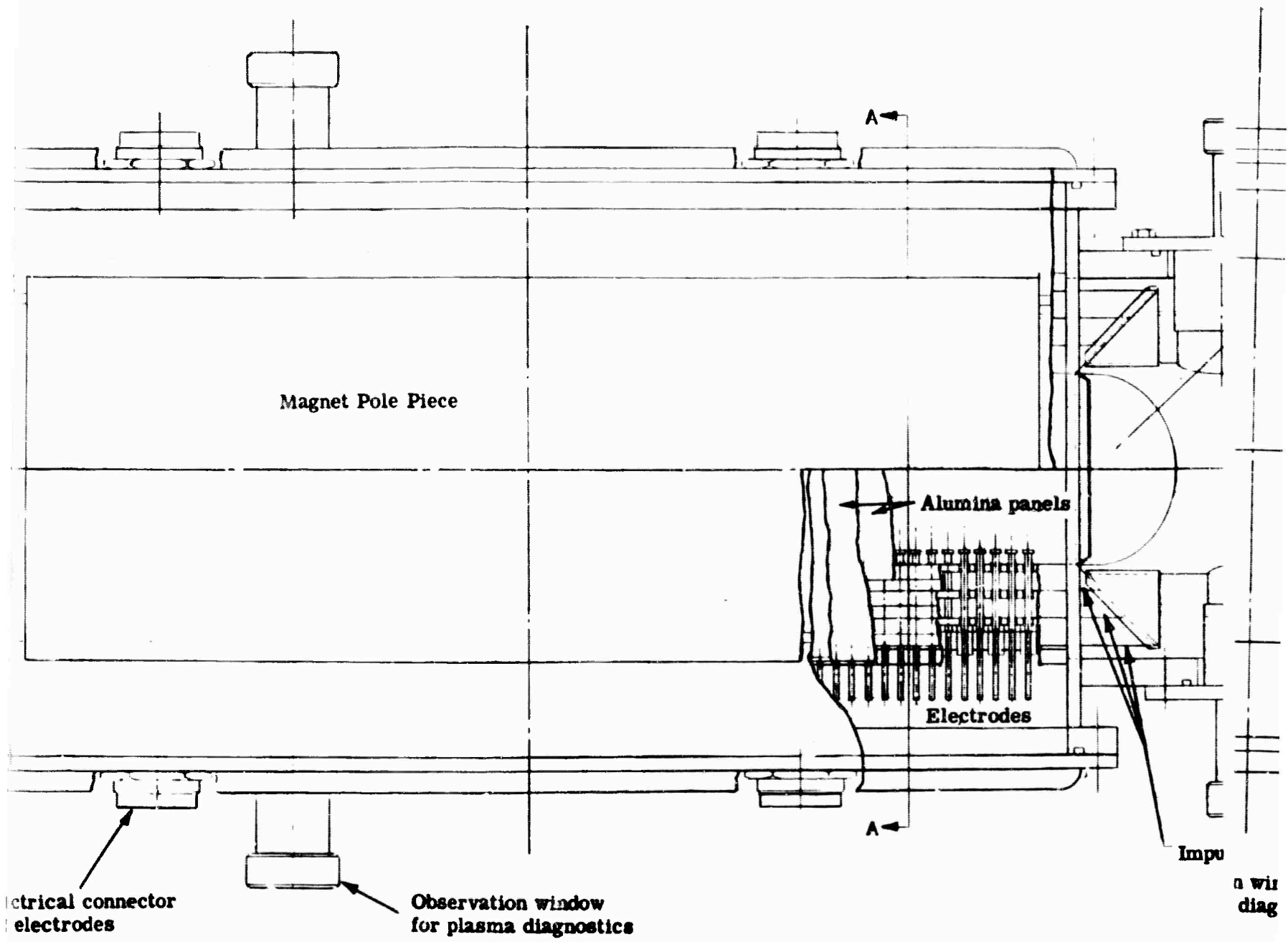
The difference between gas temperature and wall temperature in the heater section is not expected to be more than 200°K. All high temperature parts of the heater are made of tungsten to minimize metal vapor pressure.

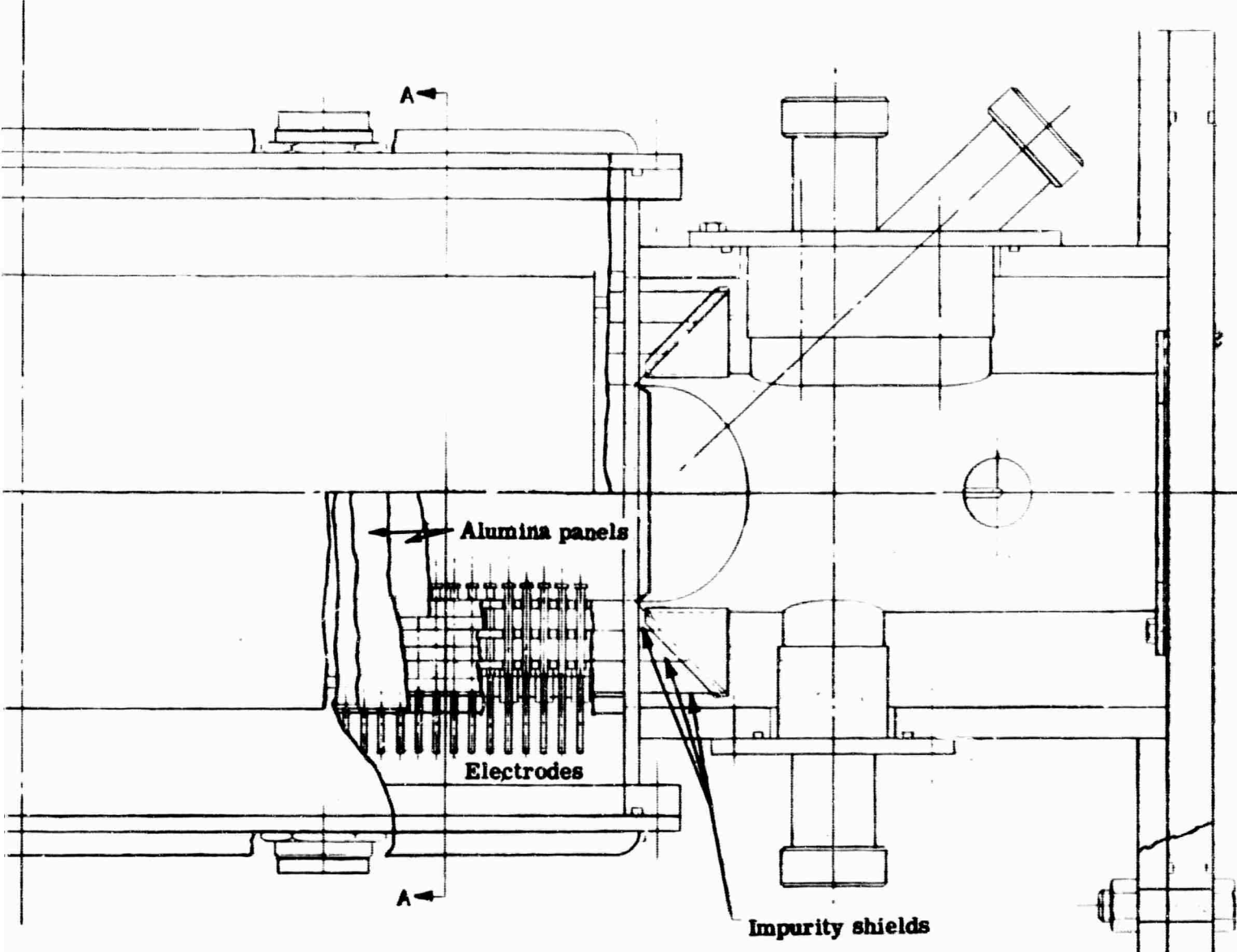
Following are the technical data concerning the helium heater:

- Maximum power input—180 kw
- Design current—3000 amp/phase, three-phase, ac
- Design voltage—20 v, three-phase, ac



A





on window
diagnostics

Figure 3. Side view of the MPD test section.

C

Allison

A three-phase regulated transformer is used having the primary winding for 440 v. The voltage output on the secondary is 0 to 35 v. The transformer is rated at 200 kva.

Figure 6 shows a photograph of the completely assembled MPD power generator research device. Design data for the MPD power generator system are presented in Table I.

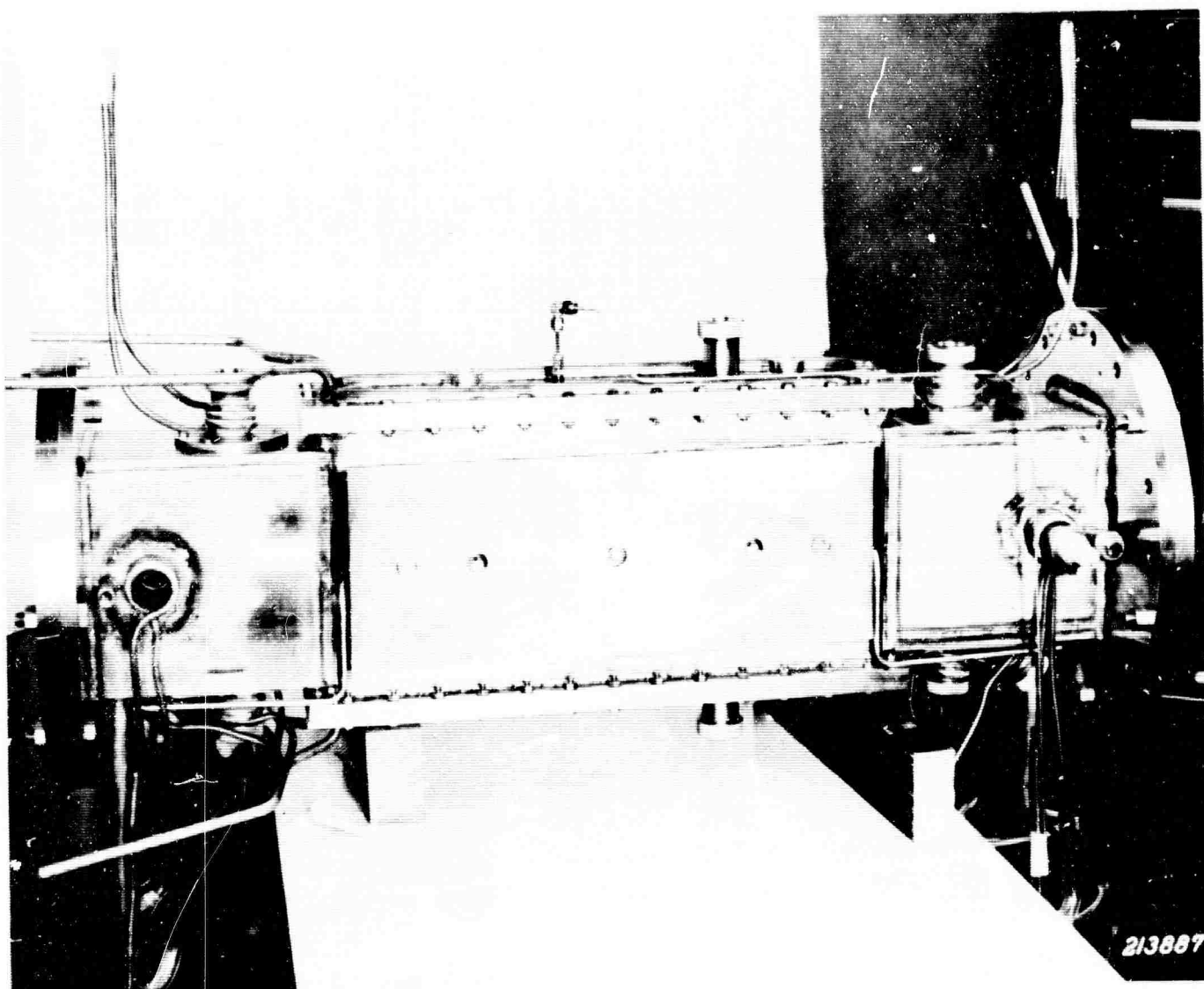


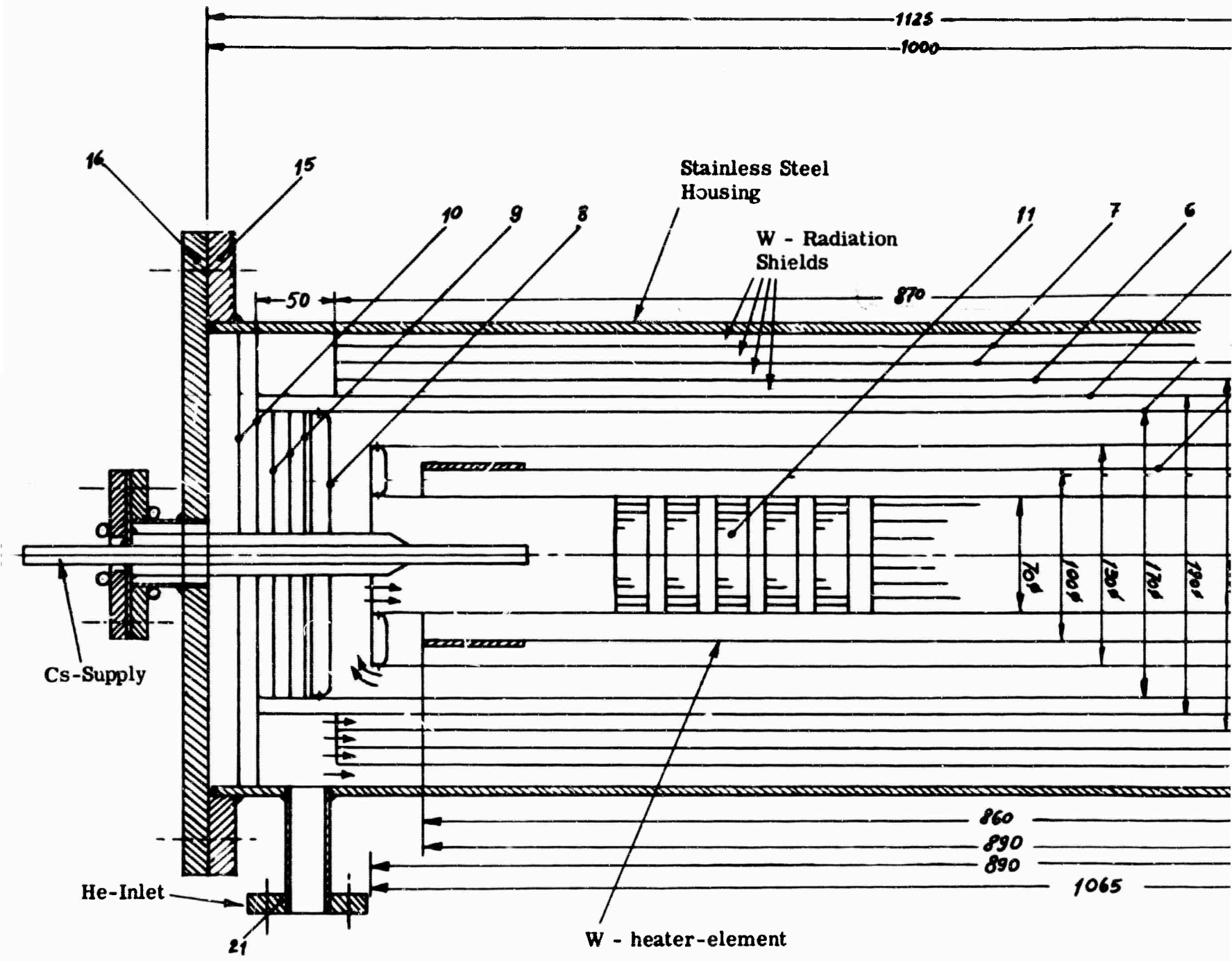
Figure 4. Generator duct with magnet pole pieces attached.

Allison

Table 1.
MPD power generator design data.

Working fluid	Helium
Pressure range	0.5 to 2.5 atm
Seed	Cesium
Seeding methods	Cesium boiler and superheater
Mass flow	Up to 30 gm/sec helium with two pumps parallel Up to 15 gm/sec helium with one pump
Heater power input—gross	180 to 200 kw (maximum)
Heater voltage	20 v, three-phase, ac
Heater current	3000 amp/phase
Duct length	50 cm
Electrode distance	7.5 cm
Channel width	2 cm
Number of electrode pairs	Up to 67
Segmentation of electrodes	0.75 cm (center-to-center)
Electrode width	0.5 cm
Electrode materials	Porous tungsten Philips electrodes type A Philips electrodes type B
Magnetic field strength	2.15 Tesla (maximum)

E



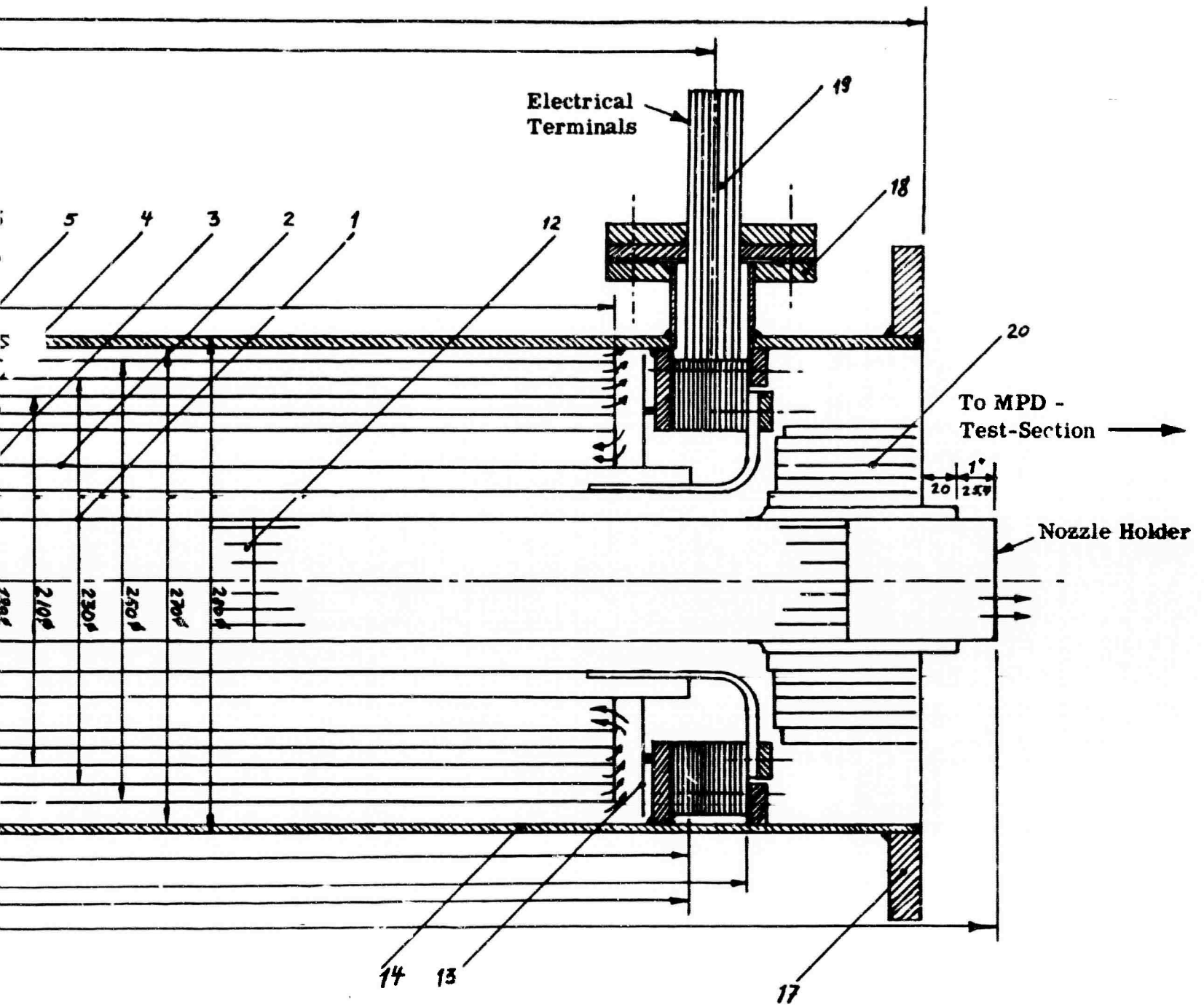


Figure 5. Schematic of the heater (Technische Hochschule drawing).

Allison

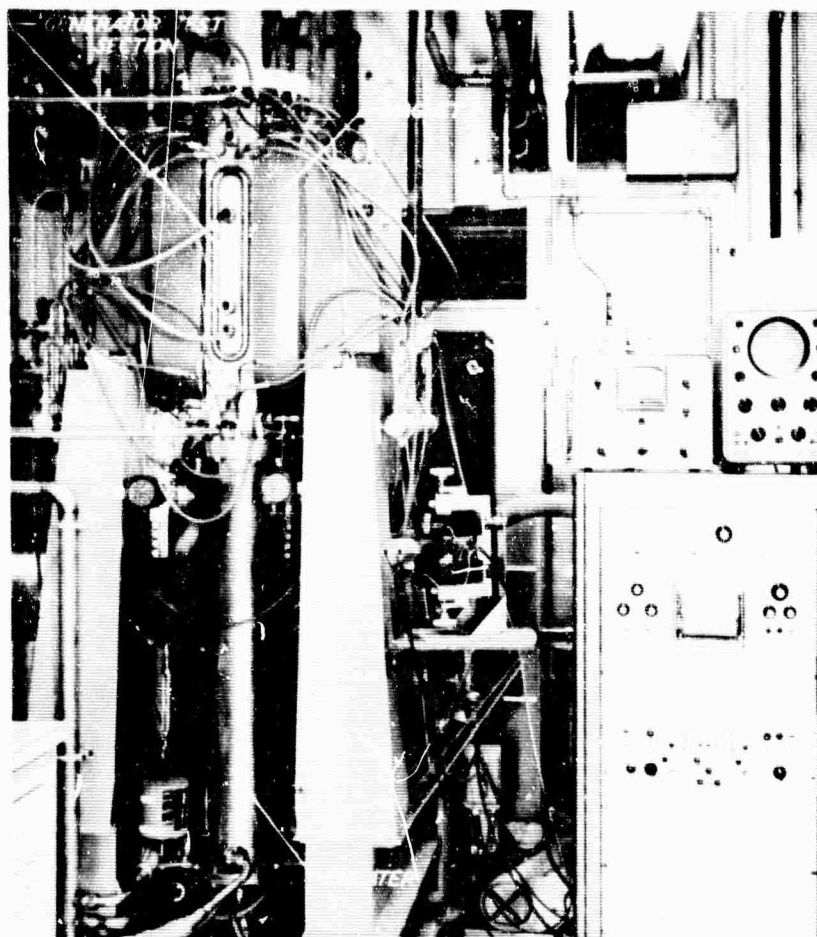


Figure 6. Assembled MPD power generator.

III. MPD GENERATOR CHECKOUT RUNS

The objective of the checkout runs is to establish calibration curves which allow predetermination of the operating conditions for an actual cesium run. Also, they serve as an endurance test with regard to determining system limitations and weaknesses, thus reducing the chance for a failure during an actual cesium run.

The accumulated running time of the new system is 228 hr to date. Only about 5% of this time, however, was actual cesium runs. The calibration curves established during the checkout runs consist of heater power input versus gas temperature, with mass flow and pressure as parameters. Thermocouples and optical pyrometry were used for measurement of the gas temperature.

Most of the checkout runs were made at the 1250, 1340, and 1450°K levels. The longest run made at a specific temperature (1340°K) without changing flow rate or any other condition lasted 2 hr. (Endurance runs at lower temperatures were often made overnight without observation.)

The generator duct was disassembled only once during the accumulated running time of 228 hr—this was to make minor modifications, not because of a failure. The heater has not been disassembled at all to date. These endurance runs show, therefore, that there are no materials and design problems at the temperature levels encountered to date and indicate that temperature levels of 1500°K are possible.

The magnet was operated up to a maximum field of 21,500 gauss. This value was measured with the test section in place employing three different gauss meters. Two of the gauss meters had solid-state sensors (Hall generators) and the third had a rotating coil. The values obtained agreed within 5%. Since it is impossible to have a gauss meter installed when running under hot conditions, a calibration curve of magnet current versus field strength was established. This curve is fed into an analog computer, and magnet current measured during a run is converted continuously into magnetic field. Therefore, all machine-plotted curves presented in this report have a linear scale for magnetic field.

The effectiveness of the cavity design—designed to reduce electrical shorting—was also tested during the endurance runs. For unseeded runs the resistance between opposite electrodes was never less than 0.1 megohm. This was also true for most of the seeded runs. Following quick shutdowns after seeded runs, electrode resistances as low as 1000 ohms were observed. Upon reheating, however, the electrode resistance returned to normal values. It is concluded, therefore, that cesium vapor condensed in the cavities and formed a conducting film. When the system was reheated, this film evaporated. It was possible to keep all other metal vapors from forming a continuous film.

Allison

During the unseeded endurance runs, outputs in the millivolt range were observed. These outputs are not considered to be MPD generator outputs because they were independent of velocity and the absolute value of the magnetic field. This output was 5 mv per electrode pair at room temperature and went up to 50 mv at high temperatures. The internal impedance of the system was about 1 megohm; therefore, the millivolt outputs never disturbed any MPD measurements. They were useful, however, for instrumentation checkout. An exact explanation for this millivolt output cannot be given as yet. It can be stated, however, that it is not an electrical pickup from the heater or any other external voltage source, since it has also been observed with all power shutdown.

The impurity level in the helium gas was continuously monitored by an oxygen analyzer and an electronic hygrometer. The oxygen level was maintained near 1 ppm and the water vapor near 25 ppm.

In addition to the work previously described, effort was initiated to measure all impurities with a mass spectrometer. The gas inlet to the mass spectrometer was designed to permit continuous sampling of the working fluid. Since the relationship of the composition of the gas in the mass spectrometer and the sample to be analyzed must be known, a viscous leak design following that of Halsted and Nier⁵ was selected. With this type of inlet design, the sample is introduced from a high pressure region (approximately 1 atm or more) directly into the mass spectrometer, which must operate at approximately 10^{-5} torr or less.

The gas inlet consisted of a type 316 stainless steel capillary tube 1.5 meters long with an ID of 1.78×10^{-4} meter. A constriction was placed in the capillary at the entrance to the mass spectrometer and was adjusted so that the pressure in the mass spectrometer was approximately 1×10^{-5} torr. A resistance heater, consisting of thermocouple wire, was placed around the capillary to prevent condensation of the working fluid constituents within the capillary tube.

The mass spectrometer was a General Electric Model 22 PC Partial Pressure Analyzer with a Model 22PT 110 type 304L stainless steel analyzer tube. The tube was modified to permit introduction of the gas sample in the immediate vicinity of the ion cage. This modification eliminated the uncertainty resulting from the long path diffusion normally used in this tube.

Halsted and Nier⁵ have shown that a multicomponent gas flowing through a viscous leak of the type previously described follows approximately the relationship

$$\frac{I_a}{I_b} = \left[\frac{M_a}{M_b} \right]^{1/2} \frac{P_a}{P_b}$$

as the upstream pressure becomes large.

Allison

In the equation,

- I = mass spectrometer current
M = molecular weight of component
P = component partial pressure in main gas stream
a and b = identify components

Systematic surveys of gas samples were made covering the mass number range from 2 to 132. A cross-check of the results was made by comparing mass number 32 data with information obtained from a Lockwood and McLorie Oxygen Analyzer. Ratios of readings taken at different times from the two instruments never varied by more than a factor of 3.

Recordings showing the helium and oxygen ion currents for both gettered and nongettered samples were made. Partial pressures for oxygen and helium as calculated from the Halsted-Nier equation are as follows:

<u>Gettered</u>	<u>Nongettered</u>
$P_{He} = 917 \text{ torr}$	$P_{He} = 886 \text{ torr}$
$P_{O_2} = 6.5 \times 10^{-2} \text{ torr}$	$P_{O_2} = 1.02 \times 10^{-1} \text{ torr}$
$\frac{P_{O_2}}{P_{He}} = 7.08 \times 10^{-5}$	$\frac{P_{O_2}}{P_{He}} = 1.15 \times 10^{-4}$

BLANK PAGE

Allison

IV. HELIUM-CESIUM RUNS

He-Cs runs were made at 1250, 1340, and 1450°K. The He mass flows varied between 10 and 13 gm/sec. The pressure in the duct was varied between 1 and 1.3 atm. The maximum value of the magnetic field was 2.15 Tesla.

Figure 7 shows a plot of open circuit voltage versus magnetic field—the theoretical vbd (voltage, magnetic field, electrode distance) curve is indicated. The leakage resistance for the run plotted in Figure 7 was 1 megohm. Also, the run was made with an extremely high seeding ratio ($>2\%$). However, as soon as the seeding ratio was reduced to a moderate level and the leakage resistance dropped to 0.1 megohm, the saturation effect observed in earlier runs re-occurs. To date it has not been possible to distinguish which of the two effects (leakage resistance and seeding ratio) causes the saturation effect. Additional runs are required before a decision can be made. Figure 8 shows a typical curve of voltage versus magnetic field. These curves are reproducible, as has been shown by numerous runs.

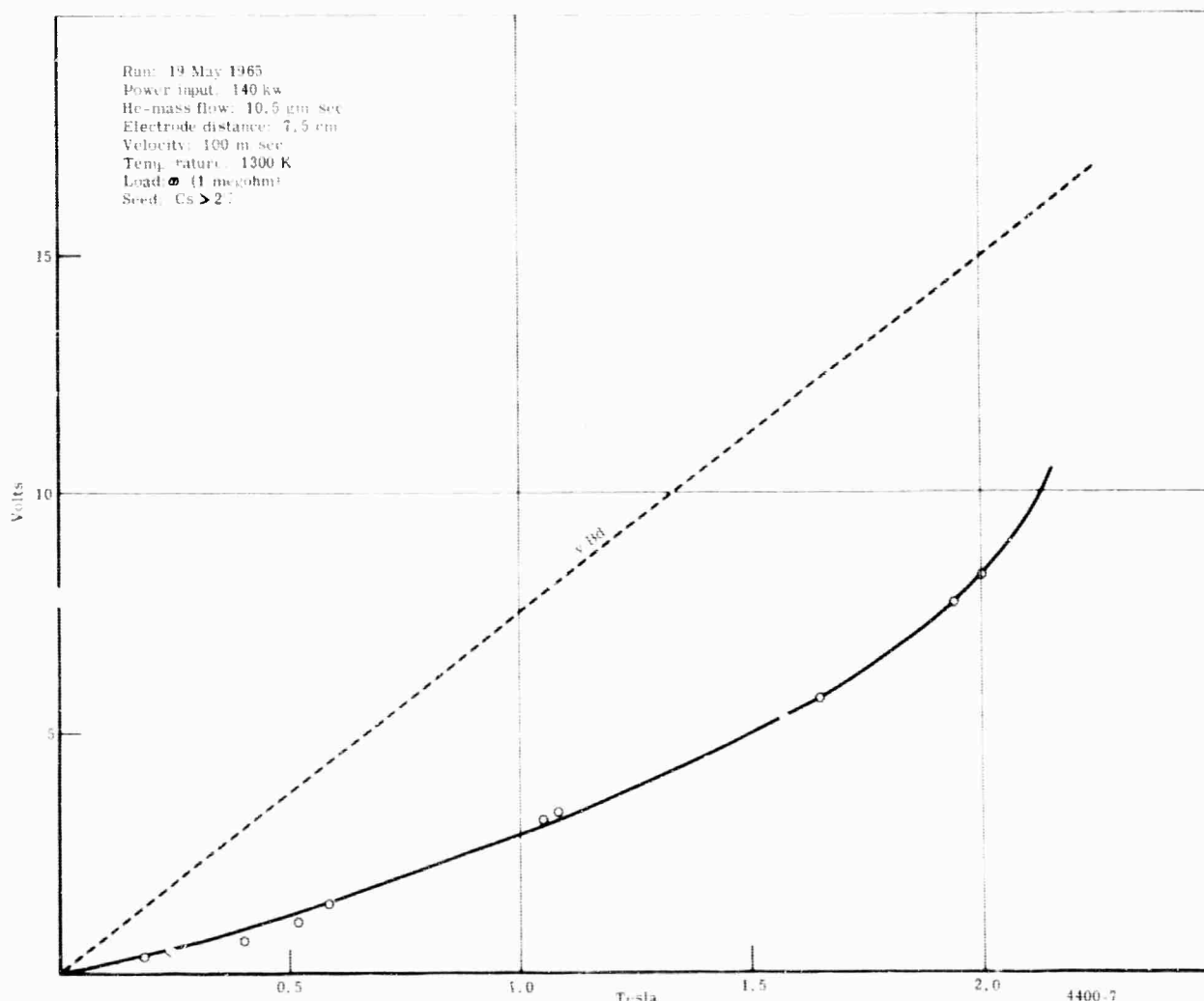


Figure 7. Oper. circuit voltage vs magnetic field—seeding $>2\%$.

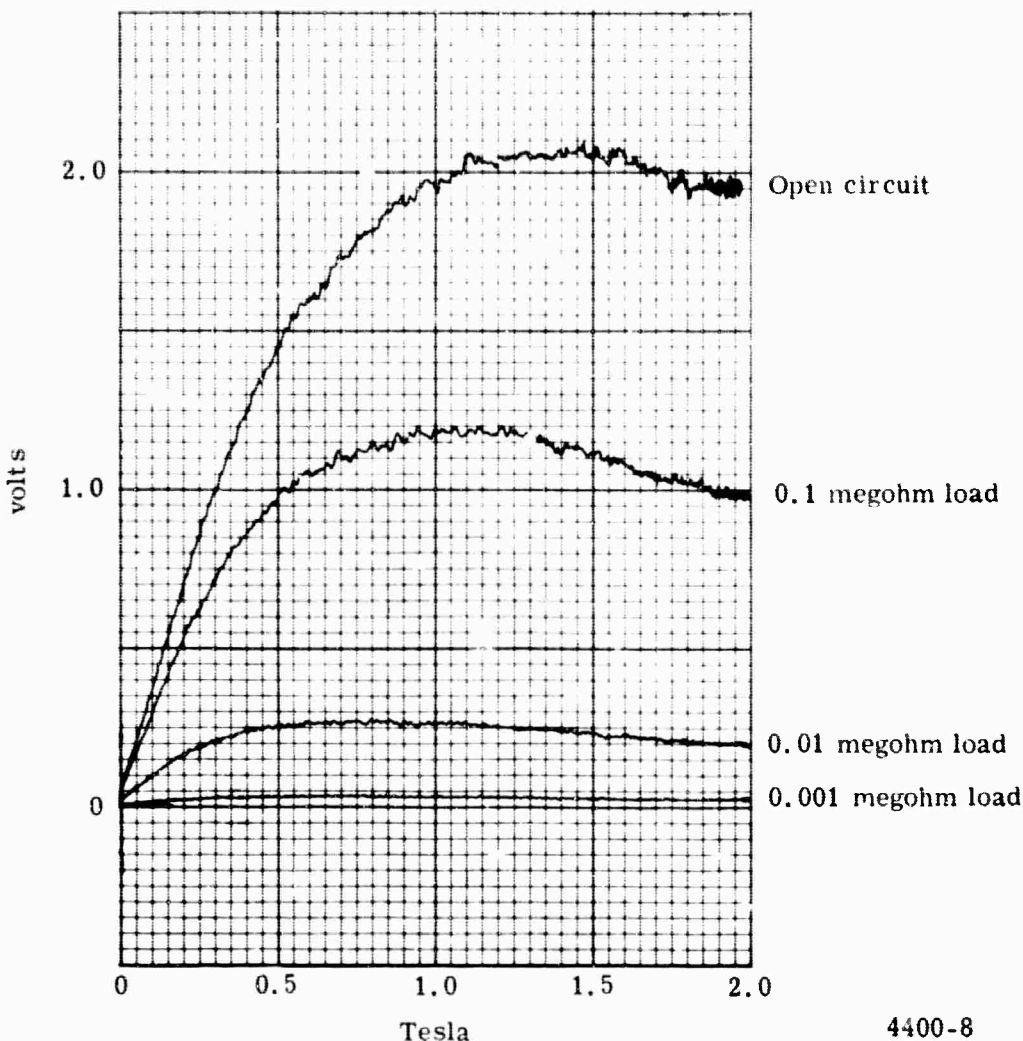


Figure 8. Reduced seeding ratio and 100 kilohm leakage resistance.

In the He-Cs runs, the open circuit voltage has been reduced considerably. The magnetic field has a saturation effect, and as the magnetic field increases above approximately 1.5 Tesla, the open circuit voltage decreases. Figure 8 was plotted directly with an x-y plotter during the run.

Figure 9 was plotted to show the pronounced decrease in open circuit voltage in the 2-Tesla region.

To show the saturation effect with respect to the influence of the Hall effect, open circuit voltage was recorded using different electrode lengths. The electrode length was increased by connecting electrode segments together electrically. The results of this run are shown in Figure 10. The test starts with curve No. 3, which indicates that electrode No. 3 was connected to the x-y recorder. The next curve, called No. 3+4, indicates that electrodes No. 3 and 4 are connected, forming one electrode twice the length of the one shown in curve No. 3, etc. The scale factor was changed by a factor of two for the lower three curves in Figure 10.

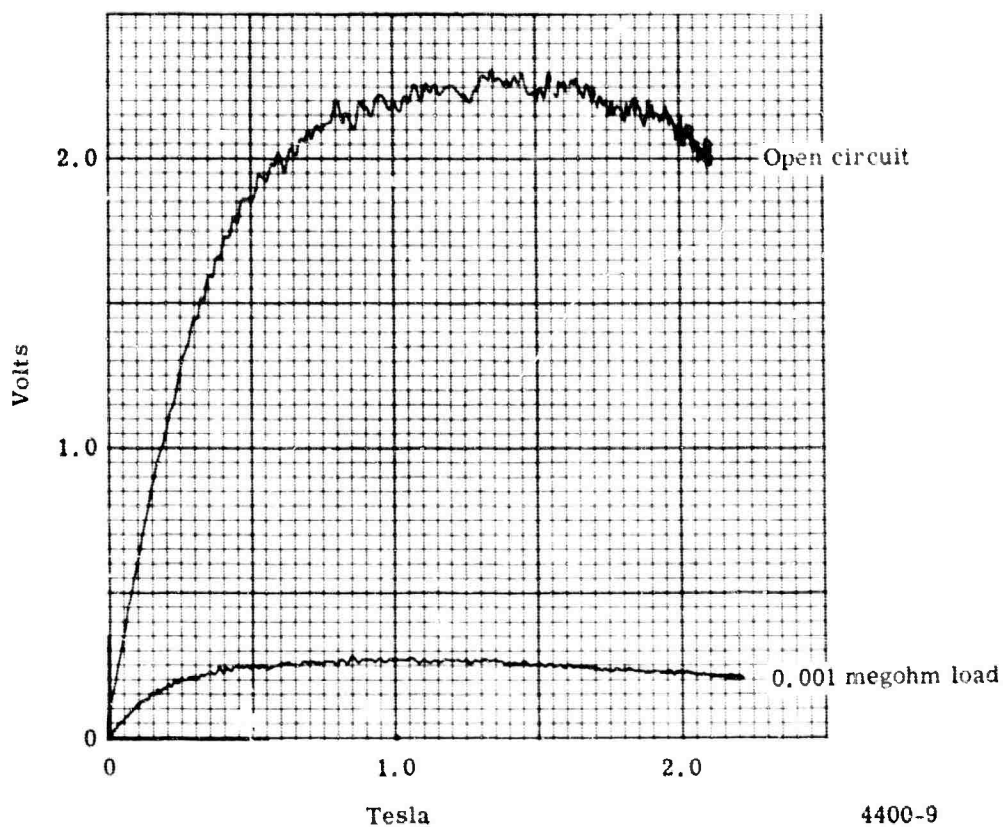


Figure 9. Curve showing pronounced decrease in open circuit voltage above 2 Tesla.

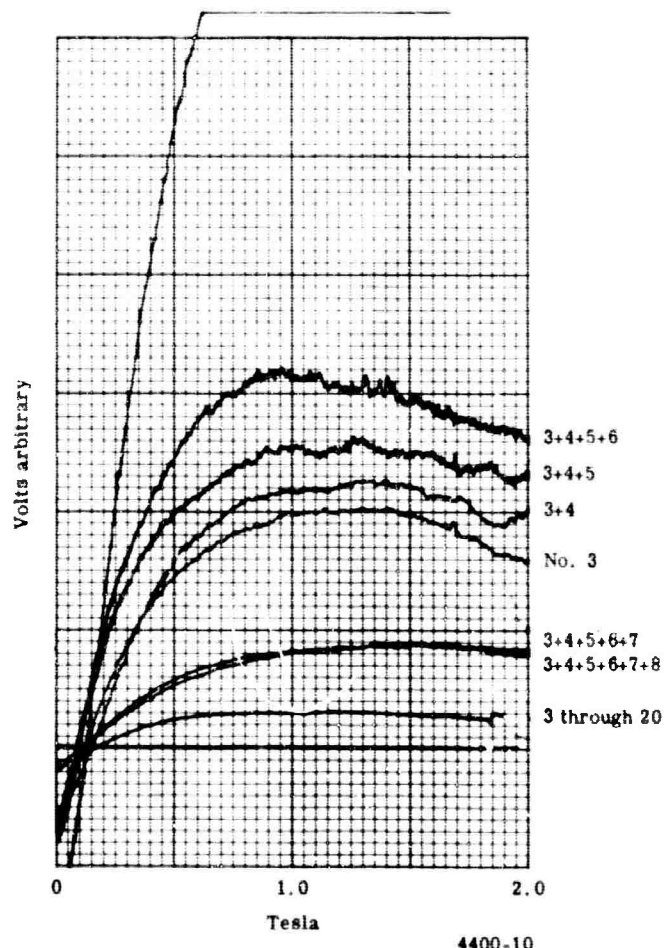


Figure 10. Output voltage for various electrode lengths.

Allison

As shown in Figure 10, lengthening the electrode altered the shape of the curve only slightly. This slight change might be attributed to the varying load. Therefore, it can be concluded that the Hall effect is not the dominant cause of the saturation effect. Since each electrode pair has a different leakage resistance, and since these leakage resistances became parallel when the electrodes were lengthened, each curve was taken at a different effective load. The effect of different loads on the saturation curve is shown in Figure 8.

As mentioned previously, the saturation effect can be overcome by increasing the seeding ratio. Figure 11 shows two curves—one taken with a seeding ratio $< 2\%$ and one taken with a seeding ratio $> 2\%$. The curve with the smaller seeding ratio shows saturation, while the curve with the larger seeding ratio shows no saturation, although it is not considered to be a good curve because the cesium mass flow was fluctuating. Thus, the saturation effect shows up only on runs with moderate or small seeding ratios.

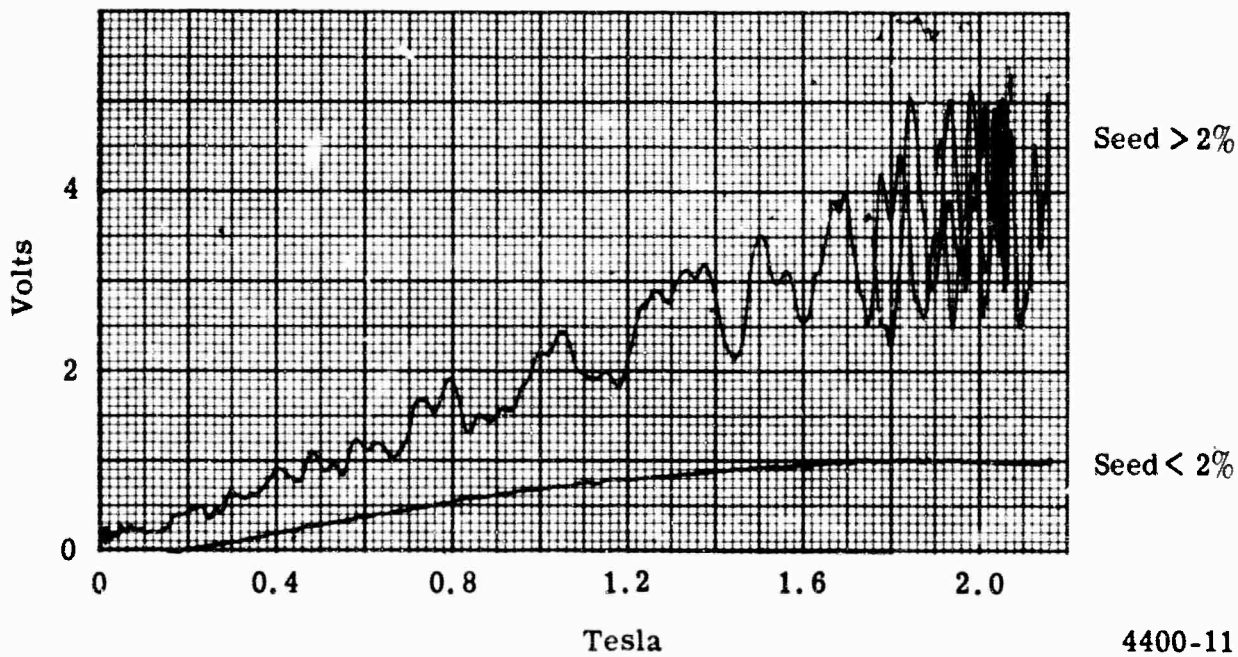


Figure 11. Saturation overcome by increasing the seeding ratio.

Allison

To date, it has not been possible to run I-V curves in the nonsaturated operating mode (Figure 7). However, a number of I-V curves were obtained in the saturated mode (Figure 8).

A typical I-V curve for the saturated mode is shown in Figure 12. The straightness of the lines indicates that no electron heating was observed. It is believed that in the nonsaturated mode, however, electron heating could be observed. This information will be obtained during the next series of tests.

In addition to the x-y plots, the data from the runs made during the report period were also recorded with an eight-channel strip chart recorder. One channel was used for magnetic field, one for helium mass flow, and the remaining six were used to plot the time behavior of six different electrode pairs selected from all parts of the generator duct. Figure 13 shows a typical strip chart recording. The saturation effect is shown by the coincident lines of maximum magnetic field and minimum voltage output of the electrodes. Equally important in the recording is the fact that the shape of the saturation curve does not change when going from one location in the channel to another. This also indicates that no motion-induced nonequilibrium ionization was observed.

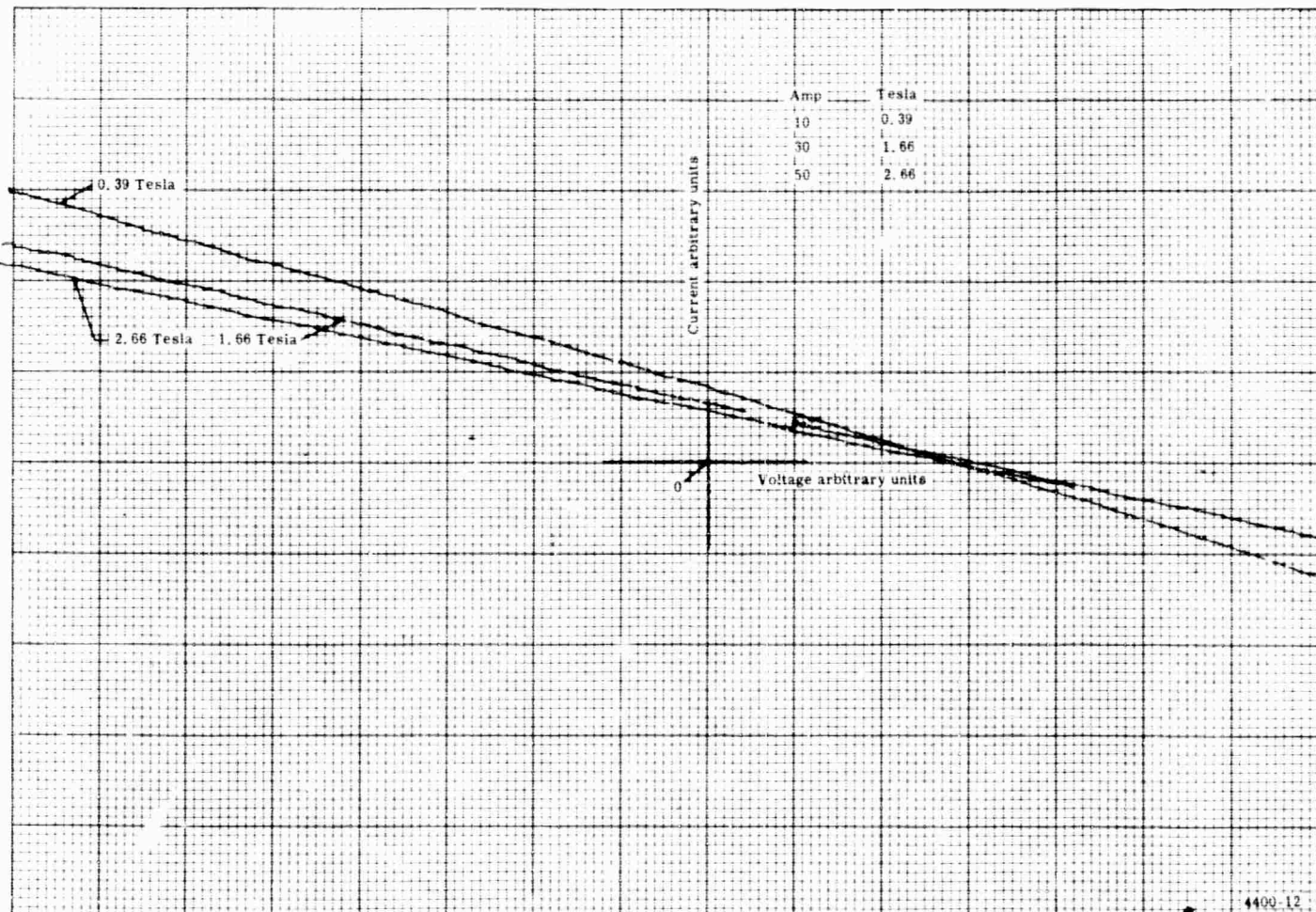


Figure 12. Typical I-V curves in saturated mode.

Allison

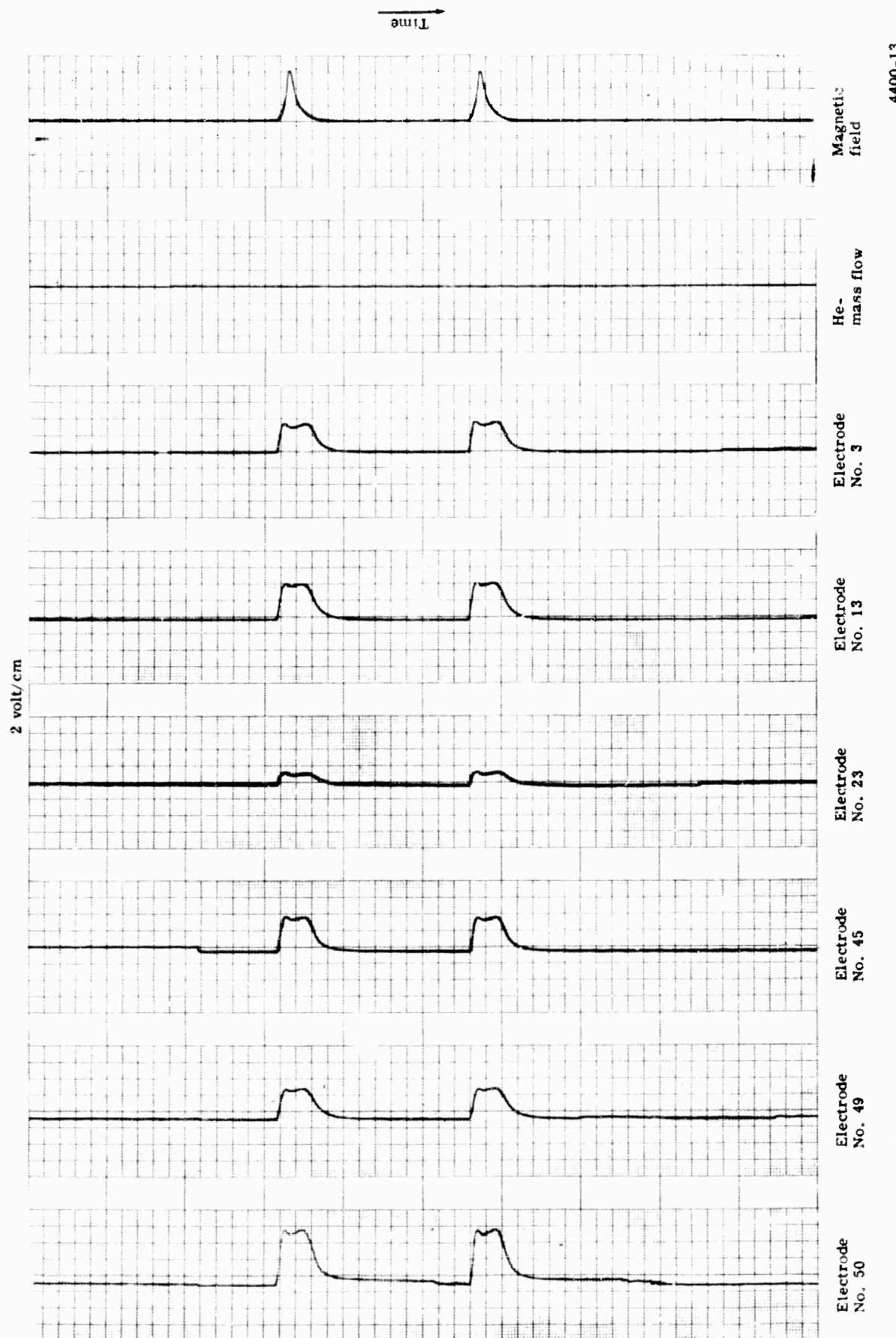


Figure 13. 8-channel strip chart data recording.

Allison

The electrodes for the runs were numbered progressively starting with No. 1 at the channel entrance. In most of the runs, output voltage increased with electrode number, as shown in Figure 14. The increase in output voltage is a result of an increase in gas velocity due to viscous effects. A theoretical curve which takes this viscous effect into account is also shown in Figure 14.

Finally, an attempt was made to measure Hall voltages. The results are shown in Figure 15. The voltage between neighboring electrodes was of the same magnitude as the voltage between opposite electrodes—it was much too low to cause a breakdown between neighboring electrodes. When connecting the electrodes in the Hall mode, the Hall voltage observed was less than 1 mv between two neighboring electrodes.

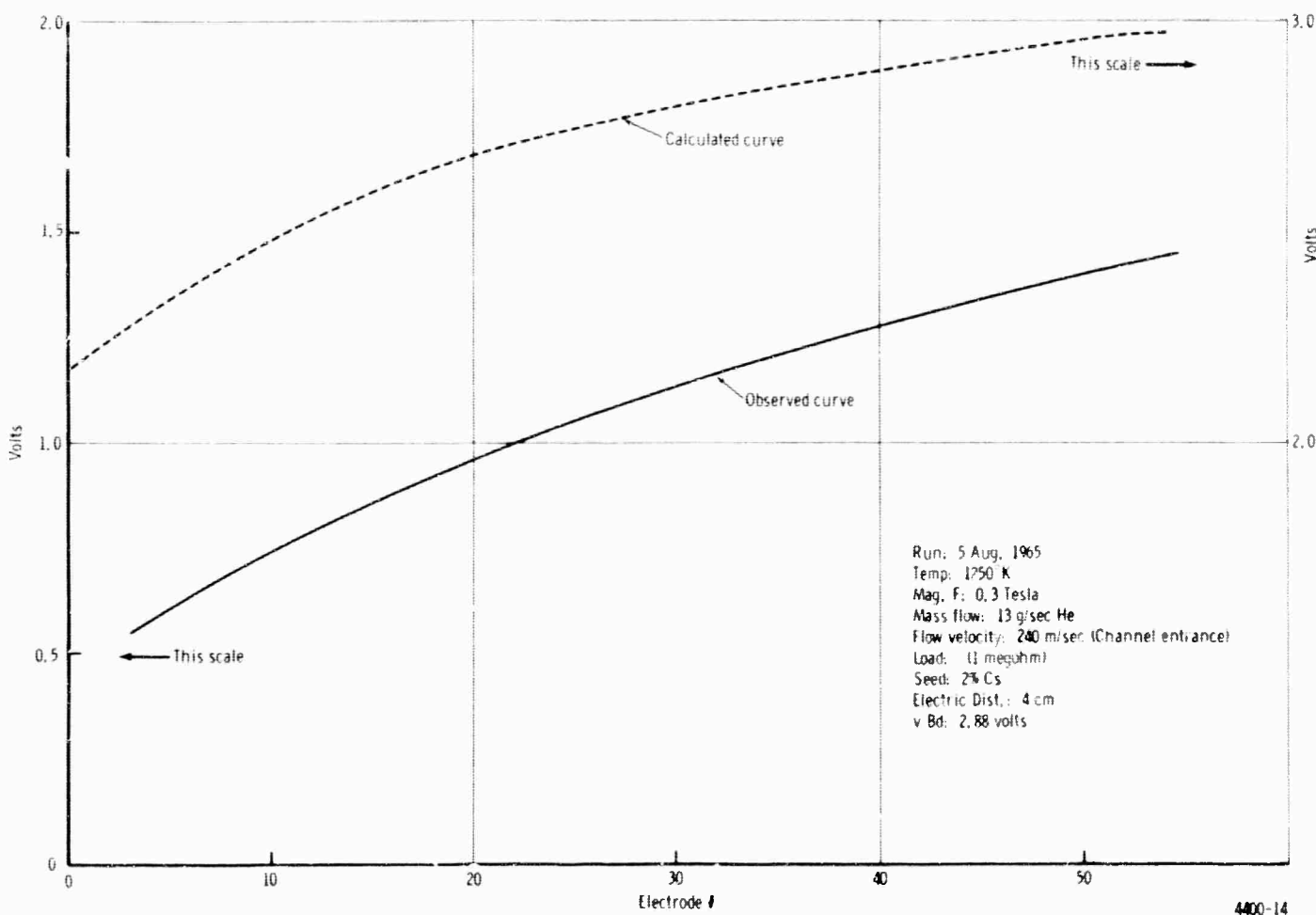


Figure 14. Comparison of theoretical and observed curves of output vs electrode numbers.

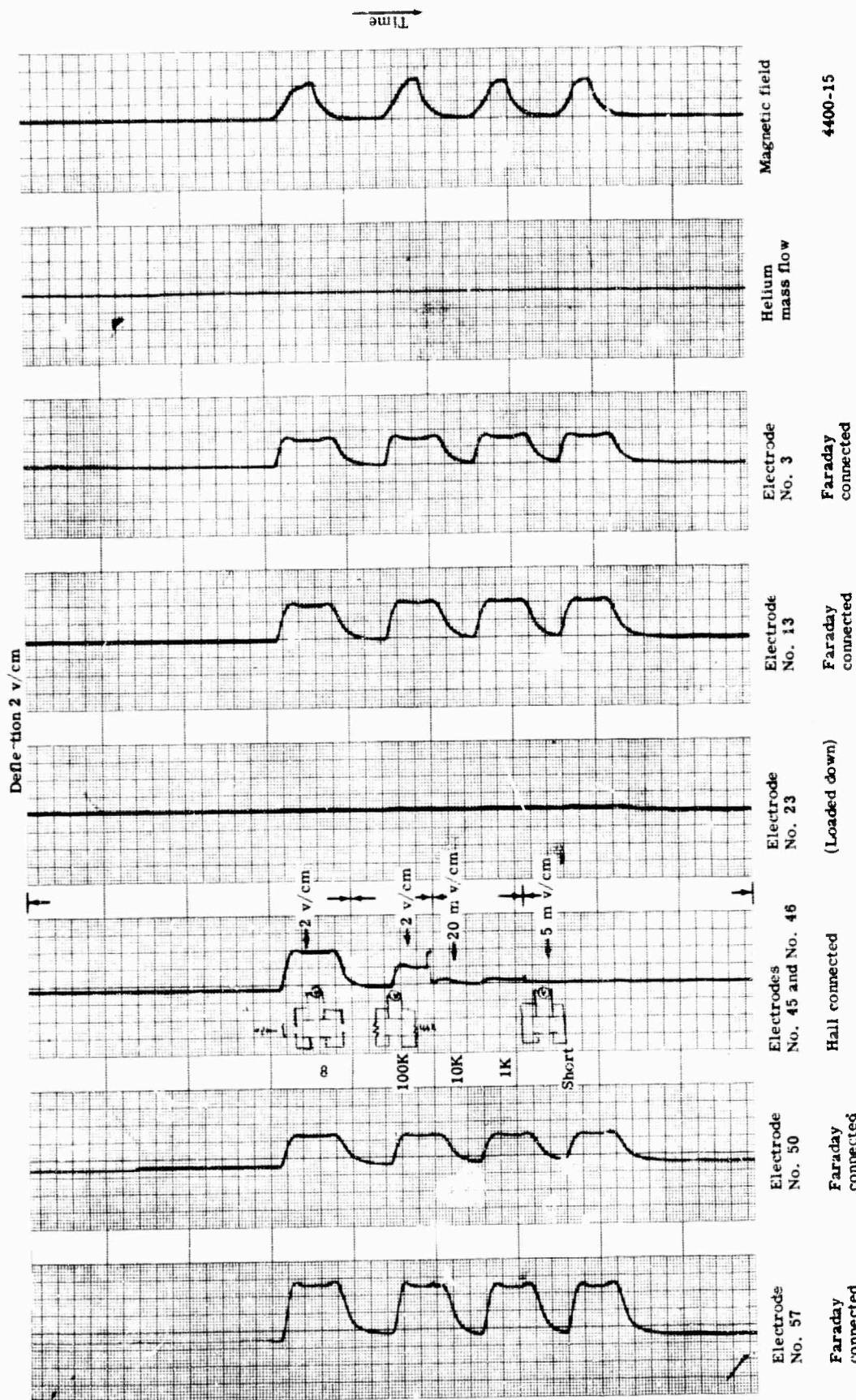


Figure 15. 8-channel measurement of Hall voltages.

V. DISCUSSION OF RESULTS

Based on the experimental results given in the preceding sections, two questions remain unanswered. First, why is the theoretical open circuit voltage not observed in the two operational modes? Second, how can the saturation effect be explained? This section discusses these questions.

It has been determined experimentally that the Hall effect does not cause the saturation effect (Figure 10). Other mechanisms that could cause this effect must, therefore, be found. One of the mechanisms could be a velocity profile over the cross section of the channel, as shown in Figure 16. As a result, the generated emf would vary across the channel. For this mechanism an electric field, E' , is impressed on the channel by the load resistor or the open circuit. In the case of the open circuit, E' is equal to the peak value of emf in the center of the channel. Since the electrode extends across the channel, E' is also extended across the channel. However, a smaller emf counteracts this E' in the proximity of the channel wall. Thus, there is current flowing in the proximity of the wall driven by $\text{emf}' = \text{emf}_{\text{wall}} - E'$. Since $\text{emf}_{\text{wall}} < E'$, the current flows in the opposite direction of any current generated in the center of the channel. Figure 16 illustrates this condition.

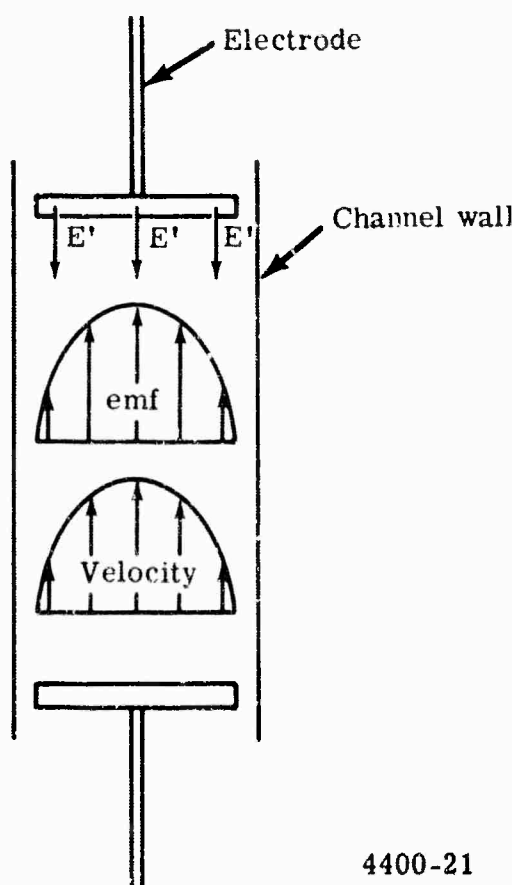


Figure 16. Velocity and emf profile across channel.

For the case of external open circuit, a current as previously described flows through an internal resistance R_{IS} (profile). This resistance can be of the same order of magnitude as the internal resistance R_I since it involves the same gas and comparable conductivity. Figure 17 shows that if $R_I = R_S$, the open circuit voltage, $V_{observed}$, would be only 50% of the true open circuit voltage (which is approximated in Figure 7). Under these conditions, as well as at very low magnetic fields, the true open circuit voltage can never be observed. This has been confirmed by laboratory observation.

Another possibility exists for internal leakage. From Figure 16, consider the walls to be coated with a layer of conducting material and connected to one of the electrodes. The resistance between electrodes would still be high. Even though the impressed electric field, E' , now lies between the one electrode and the conducting wall, which is connected to the other electrode, the resistance R_{IS} (wall) of this gap is on the order of R_I since the gas is the same and the conductivity is comparable.

Referring to Figure 18, the situation is shown where a load resistor is applied. Since gaseous resistances are rarely constant over a wide voltage-current range, it is very unlikely that R_{IS} (profile) and R_{IS} (wall) will remain constant.

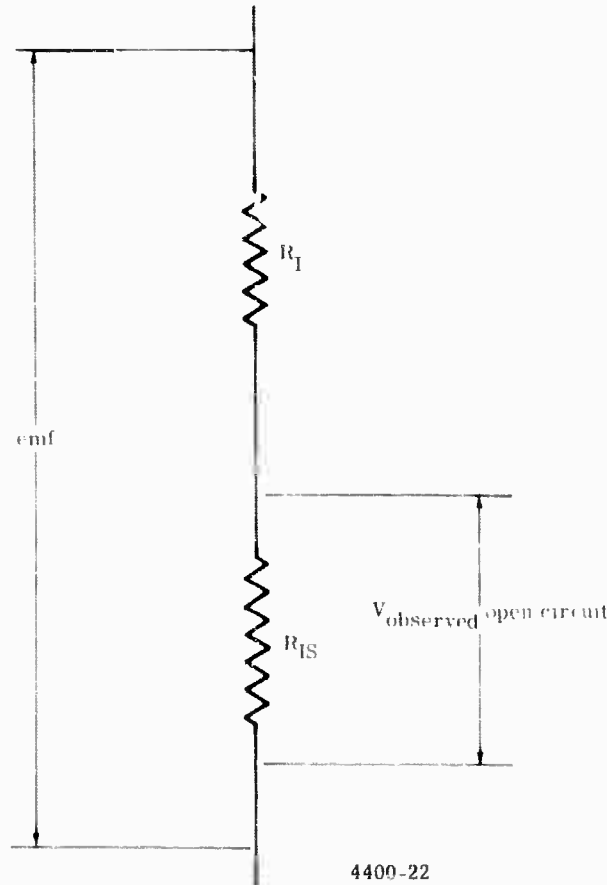


Figure 17. Schematic for internal shorting—open circuit.

4400-22

Allison

The question concerning whether or not resistance is a function of current or emf can be answered by the I-V curves in Figure 12. The curves approximate straight lines, indicating that current alone will not change R_I , R_{IS} (profile), and R_{IS} (wall). Therefore, the change in R_I and R_{IS} which causes the saturation effect must be a function of emf.

Figure 18 (right side) shows how R_{IS} (profile) and R_{IS} (wall) are affected by emf. The observed voltage is

$$V_{\text{observed}} = \text{emf}_{\text{eff}} \frac{R_L}{R_{I_{\text{eff}}} + R_L}$$

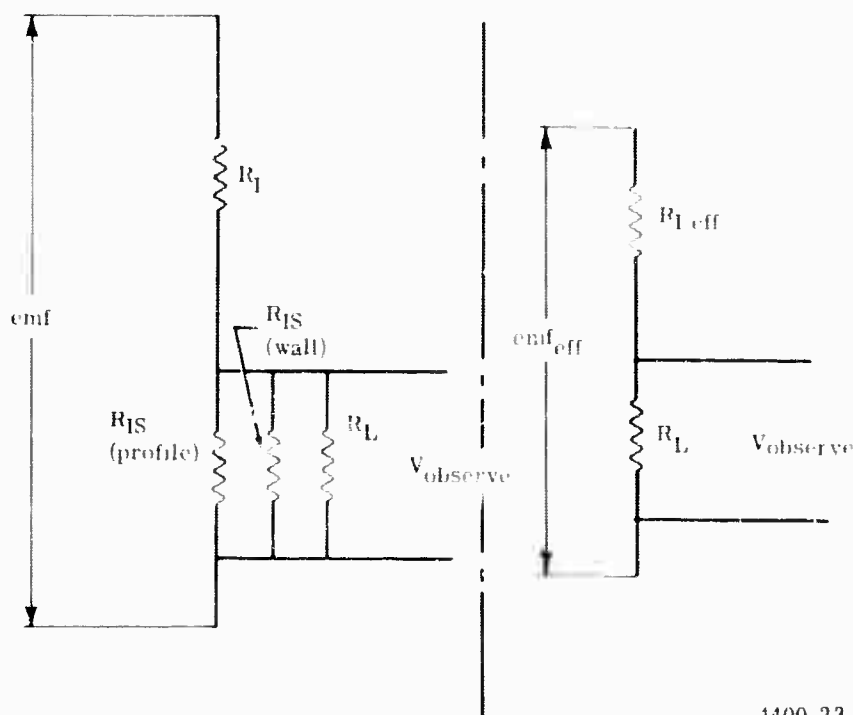
As previously stated, $R_{I_{\text{eff}}} = f(\text{emf})$. Therefore, it may be assumed that

$$R_{I_{\text{eff}}} = a E^b + c$$

and

$$\text{emf}_{\text{eff}} = d + m f$$

where a , b , c , and d are constants.



4400-23

Figure 18. Schematic for internal shorting with load applied.

Allison

Then,

$$V_{\text{observed}} = (\text{emf}) \frac{d \cdot R_L}{a(\text{emf})^b + c + R_L}$$

The observed data may be matched by proper selection of the constants a , b , c , and d . The exact values for these constants will be established and reported later.

It is desirable to distinguish between the effect of emf on R_{IS} (wall) and R_{IS} (profile). This is possible using the diagram on the left side of Figure 18. From the diagram,

$$V_{\text{observed}} = \text{emf} \frac{\left(\frac{1}{R_{ISW}} + \frac{1}{R_{ISP}} + \frac{1}{R_L} \right)^{-1}}{R_I + \left(\frac{1}{R_{ISW}} + \frac{1}{R_{ISP}} + \frac{1}{R_L} \right)^{-1}}$$

where

$$R_{ISW} = R_{IS} \text{ (wall)}$$

$$R_{ISP} = R_{IS} \text{ (profile)}$$

$$R_{ISP} = f_1 \text{ (emf)}$$

$$R_{ISW} = f_2 \text{ (emf)}$$

From the observations reported in the previous sections, it can be concluded that f_2 is a stronger function than f_1 , since an increase in wall leakage resistance seems to accompany the switch from the nonsaturated to the saturated mode.

Before a final analysis can be made, a more extensive study must be undertaken and additional data collected regarding leakage behavior so that the functions f_1 and f_2 can be firmly established.

VI. NONEQUILIBRIUM PROCESSES IN MAGNETOACTIVE PLASMA FLOWS

In a plasma to which an electric field is applied approximate local statistical equilibrium can be assumed for each component species when the energy acquired by an electron along a mean free path is small—by a factor of order $(n_{\text{electron}}/m_{\text{atom}})^{1/2}$ —compared to the thermal energy.⁶ However, the thermal equilibrium between the electron component and the atomic components is frequently disturbed, as the exchange of energy in elastic collisions between the light electrons and heavy atomic particles is extremely small.⁷ The nonisothermal plasma state is generally associated with an unusually high electron density indicating a quasi-ionization equilibrium with the electron temperature.⁸ This is observable in low pressure discharges (m. f. p. \gg plasma dimension, recombination at wall)⁹ as well as in high pressure discharges (m. f. p. \ll plasma dimension, recombination in volume).¹⁰

Instead of applying an electric field to a plasma at rest, an electric field action can be induced by moving the plasma across a region occupied by a magnetic field, whereby means of an appropriate electrode-circuit system the closing of the induced currents is provided. This leads to the concept of magnetoactive plasma flow. In contrast to the resting system in which unlimited time is available for the development of the nonequilibrium state, the time available in the steady flowing system for the development of any nonequilibrium processes is limited to the interval required for a plasma volume element to cross the magnetic field region. The plasma in the volume element changes its properties with position also due to the effect of the magnetic body force and the gasdynamic forces. Accordingly, an observer moving with an arbitrary plasma volume element would observe that the fields change with time. Considered from the moving system of reference, a steady state is not reached before the plasma volume element has left the magnetoactive region and the fields have relaxed to their thermodynamic equilibrium values.

In the following an attempt is made to investigate theoretically the complex and interacting processes in subsonic plasma flows transverse to homogeneous exterior magnetic fields. The main attention is given to the processes which lead to the buildup of nonequilibrium electron temperature and nonequilibrium electron density. The analysis is based on multifluid field equations derived from the Boltzmann equation in the 13-moment approximation.

FIELD EQUATIONS

The following analyses consider steady flows ($\partial/\partial t \equiv 0$) of low temperature plasmas consisting of a driving gas (o) with high ionization potential (in which, consequently, reactions can be neglected) and the ionization products of an easily ionizable seeding gas—seed atoms (a), seed ions (i), and electrons (e). In particular, the numerical analysis refers to a 1% cesium-seeded helium plasma initially at a pressure of $P_0 = 1.5 \times 10^5$ newton/m² and a temperature of $T_0 = 2000^\circ\text{K}$ ($\text{o} \equiv \text{He}$, $\text{a} \equiv \text{Cs}$, $\text{i} \equiv \text{Cs}^+$). For electron temperatures of the same order of magnitude

Allison

as the gas temperature, ionizations and recombinations in steps can be disregarded in the first approximation.¹¹ For the plasma, the essential reaction mechanisms are two-body electron-atom collision ionization¹² and three-body electron-ion-electron collision recombination,¹³ from and to the atomic ground level, respectively. The corresponding reaction equation is:



Introducing the stoichiometric coefficient, ν_s , of the components $s = e, i, a$, and o in accordance with Equation (1)

$$\nu_e = +2 - 1 = +1, \quad \nu_i = +1, \quad \nu_a = -1, \quad \nu_o = 0 \quad (2)$$

the reactive mass density production in the components (s) is described by¹⁴

$$\vec{v}_s \cdot \nabla n_s m_s + n_s m_s \nabla \cdot \vec{v}_s = \nu_s m_s (\Gamma^+ - \Gamma^-) \quad (3)$$

The reaction rates for ionization, Γ^+ , and recombination, Γ^- , are related to the particle densities and electron temperature by

$$\Gamma^+ = n_e n_a S_{ea}, \quad \Gamma^- = n_e n_i n_e R_{eie} \quad (4)$$

The probability coefficients for two-body (e-a) ionization, S_{ea} , and three-body (e-i-e) recombination, R_{eie} , for Maxwellian plasmas are:^{15*}

$$S_{ea} = \left(\frac{e^2}{4\pi\epsilon_0} \right)^2 \frac{\xi_n}{\epsilon_n^2} \left(\frac{2\pi k T_e}{m_e} \frac{e}{c} \right)^{1/2} e^{-\frac{\epsilon_n}{k T_e}} \cdot G \quad (5)$$

$$R_{eie} = \frac{1}{2} \left(\frac{h}{m_e} \right)^3 \left(\frac{e^2}{4\pi\epsilon_0} \right)^2 \frac{\xi_n}{\epsilon_n^2} \left(\frac{2\pi k T_e}{m_e} \right)^{-1} \frac{U_a}{U_i} \cdot G \quad (6)$$

where ξ_n = number of electrons in the highest shell n of the atom in ground state, ϵ_n = ionization energy of the atom from n -th shell, $U_{a,i} \cong 2 J_{a,i}^{(0)} + 1$ = excitational partition functions, and $G = \left(\frac{\epsilon_n}{k T_e} + \frac{3}{10} \right) / \left(\frac{\epsilon_n}{k T_e} + 1 \right)$.

*For small seeding ratios, $(n_i + n_a) \ll n_o$, the perturbation of the electron velocity distribution by the reactions can be disregarded.¹⁶

As a conclusion from Equation (3), the total mass density is conserved in the reactions,

$$\sum_s \nu_s m_s (\Gamma^+ - \Gamma^-) = 0. \quad \text{The total particle density is not conserved in the reactions,}$$

$$\sum_s \nu_s (\Gamma^+ - \Gamma^-) \neq 0, \quad \text{the trivial case of reactive equilibrium, } \Gamma^+ \equiv \Gamma^-, \text{ being excepted.}$$

When the plasma enters the region occupied by the transverse magnetic field, the charged particles are diverted into a gyration motion around the magnetic field lines, while the neutral particles are influenced indirectly by the magnetic field via collisions with the charged particles. As a consequence of the collisions of the charged particles with the neutral particles and with themselves, their gyration centers are displaced in a well defined way parallel and transverse to the flow. In the macroscopic picture, this means a drift of the plasma components relative to each other builds up spatially in these directions. For the component (s), whose particle interactions with the remaining components ($r \neq s$) result macroscopically in intercomponent friction forces [$\sim (\vec{v}_s - \vec{v}_r)$], this process is described by¹⁷

$$n_s m_s \vec{v}_s \cdot \nabla \vec{v}_s = -\nabla p_s - n_s e_s (\vec{E} + \vec{v}_s \times \vec{B}) - n_s m_s \sum_{r \neq s} \tau_{sr}^{-1} (\vec{v}_s - \vec{v}_r) \quad (7)$$

The various combinations of interactions between the charged and neutral particles in plasma are treated as Coulomb interactions [Debye-radius $D = (4\pi \sum_s n_s e_s^2 / 4\pi \epsilon_0 k T_s)^{-1/2}$ as maximum impact parameter; transport cross section $Q_{sr} = \frac{\pi}{2} (e_s e_r / 4\pi \epsilon_0 k T_{sr})^2 \cdot \ln \Lambda_{sr}$; $\Lambda_{sr} = D \left(\frac{|e_s e_r|}{4\pi \epsilon_0} / 3 k T_{sr} \right)^{-1}$ ¹⁸] and elastic sphere interactions [interaction radii r_s and r_r ; transport cross section $Q_{sr} = \pi (r_s + r_r)^2$ ¹⁹] respectively. The times, τ_{sr} , determine the relaxation of the velocity fields, and are given by

$$\tau_{sr}^{-1} = \frac{5}{3} \sqrt{\frac{2 k T_{sr}}{\pi m_{sr}}} \frac{m_{sr}}{m_s} n_r Q_{sr} \quad (8)$$

where

$$m_{sr} = m_s m_r / (m_s + m_r) = \text{reduced mass}$$

$$T_{sr} = m_{sr} [(T_s/m_s) + (T_r/m_r)] = \text{reduced temperature}$$

The electromagnetic field \vec{B} , \vec{E} acting on the plasma is composed of the exterior fields (subscript "o") and the fields produced by the motions of the charges (subscript "*"):

$$\vec{B} = \vec{B}_o + \vec{B}_*, \text{ etc. For a quasi-neutral plasma, } \vec{E} = \vec{E}_o, \text{ and}$$

$$\nabla \times \vec{B} = \mu_0 \sum_s n_s e_s \vec{v}_s, \quad \nabla \cdot \vec{B} = 0 \quad (9)$$

$$\nabla \times \vec{E} = 0, \quad \nabla \cdot \vec{E} = 0 \quad (10)$$

The omission of space charge effects is based on the presumption that the characteristic spatial extension of the plasma is large compared to the Debye shielding distance, D.

For the subsonic low temperature flows under consideration, energy transport by radiation and thermal heat fluxes [$\vec{q}_s = \vec{q}_s^{\text{radiative}} + \vec{q}_s^{\text{thermal}}$]²⁰ is not of primary importance.* The significant irreversible processes are intercomponent frictional heating [$\sim (\vec{v}_s - \vec{v}_r)^2$], inter-component scalar heat flux [$\sim (T_s - T_r)$], and reactive energy production [$\sim (\Gamma^+ - \Gamma^-)$]. Under formal inclusion of the sources of \vec{q}_s , the change of energy density in the component (s) is described by¹⁷

$$[\vec{v}_s \cdot \nabla p_s + \gamma_s p_s \nabla \cdot \vec{v}_s] (\gamma_s - 1)^{-1} = \sum_{r \neq s} \frac{T_s}{T_{sr}} \frac{m_{sr}}{m_s} \tau_{sr}^{-1} + n_s m_s (\vec{v}_s - \vec{v}_r)^2 - 3 \sum_{r \neq s} \frac{m_{sr}}{m_r} \tau_{sr}^{-1} + n_s k (T_s - T_r) - \nu_s \Delta \epsilon_s (\Gamma^+ - \Gamma^-) - \nabla \cdot \vec{q}_s \quad (11)$$

In an ionization act, the ionization energy is taken out of the electron component. In a recombination act, the binding energy of the same amount is fed into the electron component. Furthermore, with every transformed s-particle, the energy $3/2 k T_s$ is liberated in the mean. Therefore, in Equation (11), the reactive variation of energy per particle of the component (s) is given by (δ_{rs} = Kronecker δ -symbol)

$$\Delta \epsilon_s = \epsilon_n \delta_{es} - \frac{3}{2} k T_s \quad (12)$$

By summation of Equation (11) over s it can be shown—with help of Equations (3) and (12)—that the plasma as a whole exhibits a reactive energy source, $S = \epsilon_n (\Gamma^+ - \Gamma^-)$.

The equations of state for the individual components (s) are:

$$p_s = n_s k T_s \quad (13)$$

Equations (3), (7), (9), (11), and (13) form a complete set of field equations for the considered steady multitemperature multicomponent flow. The expressions for the elastic transport processes are valid for infrasonic relative drift velocities.¹⁷

$$\frac{1}{2} m_{sr} (\vec{v}_s - \vec{v}_r)^2 \ll k T_{sr} \quad (14)$$

*A discussion of the assumptions made is presented later, together with further problems.

PLASMA FLOW MODEL

Consideration is given to a parallel plasma flow of initial velocity, \vec{V}_0 , (\parallel -direction) entering at $x = 0$, a region occupied by a transverse homogeneous induction, \vec{B}_0 , extended up to $x = L$. In the directions perpendicular to \vec{V}_0 and \vec{B}_0 (\perp -direction), the flow is limited by electrodes [parallel to the plane (\vec{V}_0 , \vec{B}_0) and a distance, d , apart] which collect the induced electrical currents into an exterior circuit system. In the directions parallel to \vec{B}_0 , the flow is assumed to be unlimited.

For mathematical convenience, the following conditions are introduced, allowing the flow to be treated as quasi-one-dimensional [in which any flow field can be only a function of the axial coordinate, x : $f_s = f_s(x)$]. The magnetic stresses are assumed to be large compared to the viscous stresses. This requires, $\bar{\sigma} \bar{V} \bar{B}^2 \gg \bar{\mu} \bar{V} d^{-2}$ — i.e., Hartmann numbers²⁰

$$H = (\bar{\mu}/\bar{\sigma})^{1/2} d \bar{B} \gg 1 \quad (15)$$

Under this condition, the transverse inhomogeneities due to viscous stresses can be disregarded and the nonuniformity in the axial direction is influenced solely by the force density, $\vec{k}_{\parallel} = \vec{j}_{\perp} \times \vec{B}$, resulting from the interaction of the transverse current density, $\vec{j}_{\perp} = \sum_s n_s e_s \vec{v}_{s\perp}$, with \vec{B} . At inductions \vec{B}_0 , for which $\omega_e \tau_e \gtrsim 1$, $\omega_e = |e_e| B/m_e$, and $\tau_e^{-1} = \sum_{s \neq e} \tau_{es}^{-1}$, the resultant of the Hall-field and axial electron pressure gradient diffusion field would produce a downstream current density, $\vec{j}_{\parallel} = \sum_s n_s e_s \vec{v}_{s\parallel}$. The interaction of the latter with \vec{B} would result in a transverse force density, $\vec{k}_{\perp} = \vec{j}_{\parallel} \times \vec{B}$, perturbing the one-dimensionality. To ascertain the one-dimensionality, the resultant axial plasma field is assumed to be compensated by a field ($\vec{j}_{\parallel} \equiv 0$).

$$\vec{E}_{\parallel} = \left[\sum_s n_s e_s \vec{v}_{s\perp} \times \vec{B} - \nabla_{\parallel} p_e \right] (n_e |e_e|)^{-1} \quad (16)$$

This requires an ideally segmented electrode system, each opposite electrode pair being connected by an individual exterior circuit.²¹ Because of Equation (16), the electrical power liberated in the plasma is that of an ideal Faraday flow, $W \equiv \vec{j} \cdot (\vec{E} + \vec{V} \times \vec{B}) = \sigma (\vec{E} + \vec{V} \times \vec{B})_{\perp}^2$, where $\sigma = n_e e_e^2 \tau_e / m_e$ is the scalar conductivity. So-called end losses and their effects are ignored. These can be estimated separately.²²

For an analysis of nonequilibrium effects, it is adequate to allow for a maximum induced electric field action. For this reason, opposite electrodes are taken as short circuited by their

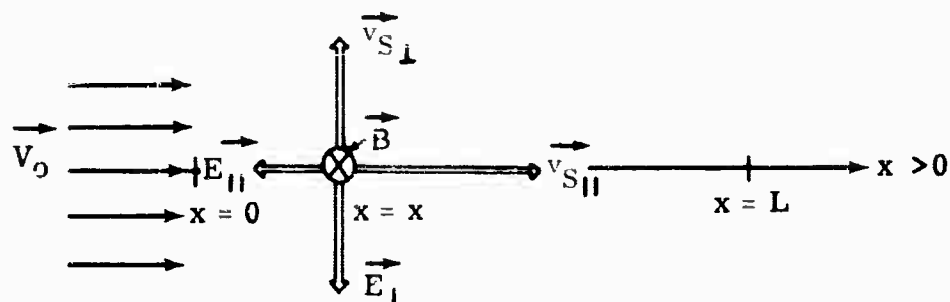
Allison

exterior circuit.* The geometry of the flow fields can now be stated as follows for the considered one-dimensional flow model (Figure 19):

$$\vec{E} = \vec{E}_{\parallel} + \vec{E}_{\perp}; \quad \vec{E}_{\perp} = 0 \quad (17)$$

$$\vec{B} = \vec{B}_0 + \vec{B}_*; \quad \vec{B}_* \parallel \vec{B}_0 \quad (18)$$

$$\vec{v}_s = \vec{v}_{s\parallel} + \vec{v}_{s\perp}; \quad \vec{v}_{e\parallel} = \vec{v}_{i\parallel} \quad (19)$$



4400-16

Figure 19. Geometry of flow fields.

For the numerical analysis, a plasma is specified which is composed of helium, cesium, and the ionization products of the latter at a seed ratio $a \equiv (n_a + n_i)n_o = 10^{-2}$. The initial ionization is taken in accordance with the Saha equation (thermodynamic equilibrium). The initial values defining the flow before entering the magnetic field region are assumed as shown in Table II. Different exterior inductions are considered— $B_0 = 2, 3, 4$, and 5 Tesla.

Table II.
Initial flow values.

Pressure— $P_o = 1.5 \times 10^5$ newton/m ²	Temperature— $T_o = 2000^\circ\text{K}$
Mach number— $M_o = 0.5$	Velocity— $V_o = 1.155 \times 10^3$ m/sec
Helium density— $n_{o,o} = 5.38 \times 10^{24}$ m ⁻³	Cesium density— $n_{a,o} = 5.38 \times 10^{22}$ m ⁻³
Electron density— $n_{e,o} = 4.24 \times 10^{19}$ m ⁻³	Ion density— $n_{i,o} = 4.24 \times 10^{19}$ m ⁻³

The elementary constants of the plasma particles are listed in Table III ($Q_{sr} = Q_{rs}$).^{24, 25}

*The case of ohmic exterior circuits, which is primarily of technical interest, has been studied in an earlier investigation.²³

Allison

Table III.
Elementary particle constants.

$Q_{eo} = 5.5 \times 10^{-20} \text{ m}^2$	$m_o = 6.540 \times 10^{-27} \text{ kg}$
$Q_{ea} = 4.0 \times 10^{-18} \text{ m}^2$	$m_a = 2.172 \times 10^{-25} \text{ kg}$
$Q_{io} = 9.0 \times 10^{-20} \text{ m}^2$	$m_i = 2.172 \times 10^{-25} \text{ kg}$
$Q_{ia} = 2.0 \times 10^{-18} \text{ m}^2$	$m_e = 9.108 \times 10^{-31} \text{ kg}$
$\epsilon_n = 3.893 \text{ eV}$	$e = 1.602 \times 10^{-19} \text{ ampsec}$

No evaluation is made of the total generated current (current density integral over the electrode plane). In this case, the numerical analysis does not require specification of the electrode dimensions, nor of the electrode distance as the exterior electric field is given.

NUMERICAL RESULTS AND ANALYTICAL DISCUSSIONS

The field equations of the one-dimensional flow model were integrated numerically for the given initial conditions. The computer program employed a second order Runge-Kutta numerical integration scheme to carry the investigation over the entire subsonic flow length—i.e., up to that point where the Mach number becomes $M = 1$. In the regions of strong field gradients an integration step size of $\Delta x = 10^{-5} \text{ cm}$ was used to ensure uniformity and accuracy.

Change of Mean Flow Fields

The interaction of the induced current density with the magnetic induction results in a force density antiparallel to the flow velocity, $\vec{k}_{\parallel} = -j_{\perp} B \vec{e}_{\parallel f}$. Therefore, the magnetic interaction has an effect on the flow, which is quantitatively similar to a viscous drag force. This effect leads to the terms "magnetic drag force" and "magnetic viscosity." Using this analogy, it is concluded that the mean plasma fields change with increasing length coordinate, $x > 0$, in a subsonic flow as follows:

a) Mean static pressure, $P = \sum_s p_s$, mean static temperature $\tau = \sum_s n_s T_s / \sum_s n_s$, and mean mass density, $\rho = \sum_s n_s m_s$, decrease.

b) Mean mass velocity, $\vec{V} = \sum_s n_s m_s \vec{v}_s / \sum_s n_s m_s$, mean dynamic pressure, $P^d = \frac{1}{2} \sum_s n_s m_s \vec{v}_s^2$, and Mach number, $M = \left| \sum_s n_s m_s \vec{v}_s \right| / \sum_s \gamma_s n_s k T_s$, increase.

Accordingly, under subsonic conditions, ultimately a transformation of potential energy or static pressure into kinetic energy or dynamic pressure takes place—in the case of an ohmic

Allison

exterior circuit, electrical energy would also be gained. In Figure 20, the quantitative development of the dynamic processes $\alpha - \beta$ is shown in the considered flow model, where B_0 is a parameter. Note that the length at which the flow becomes sonic, $M = 1$, decreases strongly with increasing induction, B_0 .

The flow behavior can be understood physically from the second law of thermodynamics. For a simple explanation, eliminate from the field equations in the one-fluid-approximation the gradient of the flow velocity ($\kappa = E_1/VB$ = load factor):*

$$\left(\frac{1-M^2}{M^2}\right) \frac{dV}{dx} = \frac{\sigma}{\rho} \left[(1-\kappa) + \Sigma \right] B^2 \quad (20)$$

where for an adiabatic flow, $\Sigma = 0$, and for a nonadiabatic flow

$$\Sigma = (\gamma - 1) \left[(1-\kappa)^2 - \frac{\epsilon_n (\Gamma^+ - \Gamma^-) + \nabla \cdot \vec{q}}{\sigma V^2 B^2} \right] \neq 0 \quad (21)$$

For the flow under consideration, the factor $[(1-\kappa) + \Sigma]$ is necessarily positive. It follows

$$M < 1: \frac{dV}{dx} > 0; \quad M > 1: \frac{dV}{dx} < 0$$

Whether a transformation of potential energy or kinetic energy takes place in the magnetoactive region depends consequently on whether the flow is initially subsonic or supersonic.

*Summation of Equations (7) and (11) over $s = e, i, a$, and o yields:

$$\rho \vec{V} \cdot \nabla \vec{V} = - \nabla P + \vec{j} \times \vec{B} + \Delta_1. \quad (A)$$

$$\vec{V} \cdot \nabla P + \gamma P \nabla \cdot \vec{V} = (\gamma - 1) \left[\vec{j} \cdot (\vec{E} + \vec{V} \times \vec{B}) - \epsilon_n (\Gamma^+ - \Gamma^-) - \nabla \cdot \vec{q} \right] + \Delta_2 \quad (B)$$

It is usual to neglect the small quantities Δ_1 , and Δ_2 ($\vec{w}_s = \vec{v}_s - \vec{V}$):

$$\Delta_1 = \sum_s n_s m_s \vec{v}_s \cdot \nabla \vec{w}_s$$

$$\Delta_2 = - \sum_s \left[\vec{w}_s \cdot \nabla p_s + \gamma_s p_s \nabla \cdot \vec{w}_s - \frac{3}{2} (\gamma_s - 1) \nu_s k T_s (\Gamma^+ - \Gamma^-) \right]$$

Equation (20) follows then from (A) and (B) by elimination, using Ohm's law in addition.

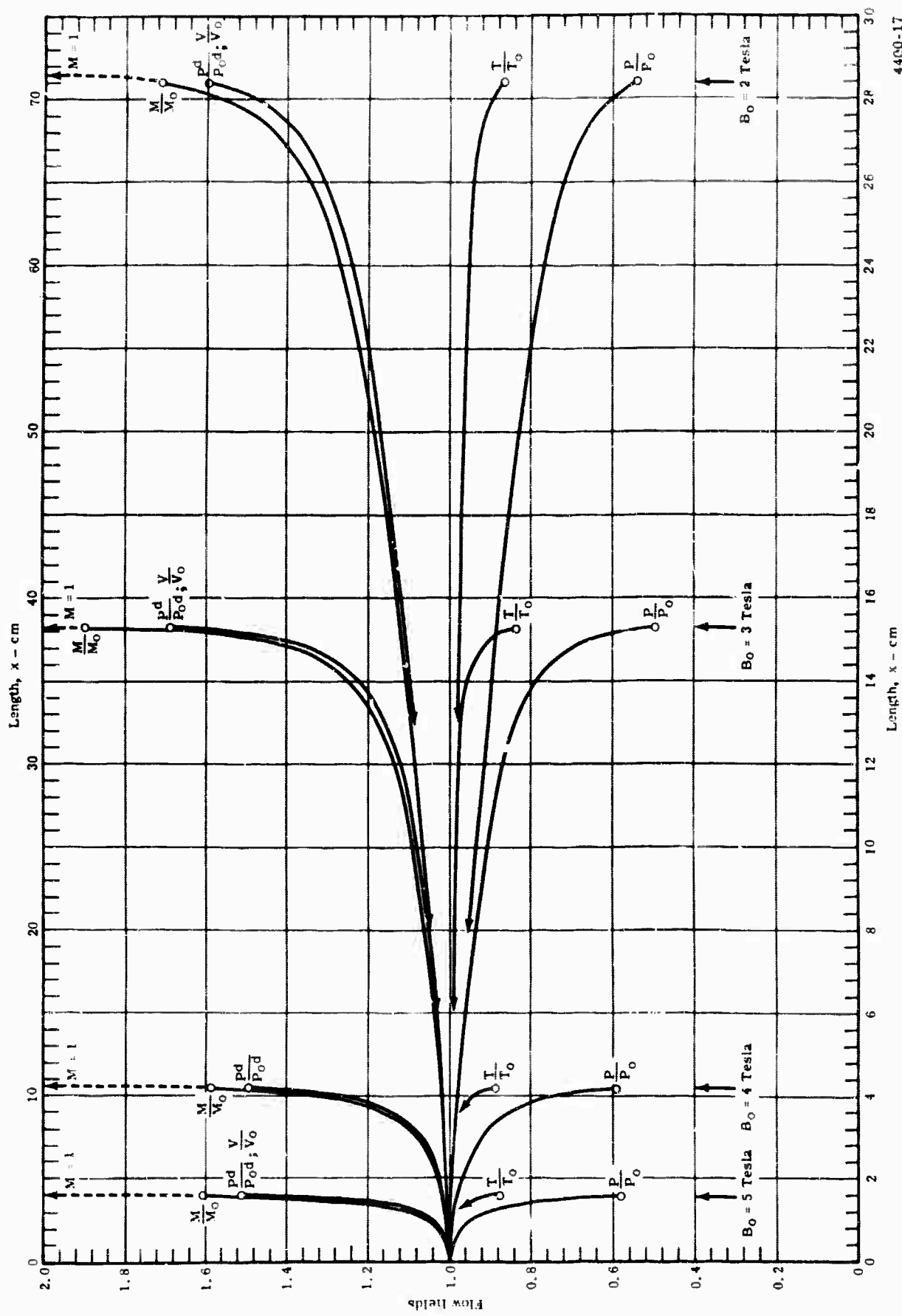


Figure 20. Mean flow fields (upper abscissa for $B_0 = 2$ Tesla).

Allison

Integration of Equation (20) from $x = 0$ ($V = V_0$, $M = M_0$) to $x = L$ ($V = V_1$, $M = M_1$) leads to the following integral equation for the length, L , at which the Mach number becomes M_1 , where consideration is made of the invariance of ρV :

$$\int_{M_0}^{M_1} \frac{1 - M^2}{M^2} \frac{dV}{V} = \frac{1}{\rho_0 V_0} \int_0^L \sigma [(1 - \kappa) + \Sigma] B^2 dx \quad (22)$$

Adapting to the conditions of the flow model by putting $\kappa = 0$, $B \approx B_0$, $\Sigma \approx (\gamma - 1)$, and integrating the left side of Equation (22) in quasi-adiabatic approximation [$dV/V = 2[\gamma^*/(\gamma^* + 1)] dM/M$, where γ^* is a quasi-adiabatic coefficient], yields:

$$L = \frac{\gamma^*/\gamma}{1+\gamma} \left[\frac{M_1^2 - M_0^2}{M_0^2 M_1^2} - 2 \ln \frac{M_1}{M_0} \right] \frac{\rho_0 V_0}{B_0^2} \cdot \bar{\sigma}^{-1} \quad (23)$$

where $\bar{\sigma}$ is a mean conductivity defined by:

$$\bar{\sigma} = \frac{L}{\int_0^L \sigma dx} / \int_0^L dx \quad (24)$$

For a given set $M_0, 1$, L is inversely proportional to the mean conductivity, $\bar{\sigma}$, and inversely proportional to the square of the induction, B_0^2 . It must be noted, however, that $\bar{\sigma}$ depends indirectly on B_0 . These elementary considerations are reflected in the numerical results, Figure 20.

Buildup of Nonequilibrium Electron Temperature

The directed kinetic energy acquired by the charged particles in the induced electric field is transformed in part into heat by intercomponent friction. As the fraction of relative energy lost by the s-particles in elastic collision with r-particles is of the order $m_s/(m_s + m_r)$, the thermal equilibrium between the various heavy particles is only weakly disturbed. The electrons, however, can dispose of the steady heat input only if their energy is relatively great compared to that of the heavy particles as the fraction of relative energy lost in elastic collisions with heavy r-particles is of the order $m_e/(m_e + m_r)$. Therefore, the electron gas heats up relative to the remaining plasma until the losses in elastic collision with particles of the other components r—which result macroscopically in scalar heat flows $\sim (T_e - T_r)$ —and other loss mechanisms balance the electron heating. This balance is established at a length, ℓ_T , which does not depend explicitly on the induction, B_0 . Above this length, $x > \ell_T$, the flow exhibits a practically constant electron temperature plateau up to that point where the Mach number begins to rise steeply, $M \rightarrow 1$. In this region, due to the strong increase of induced electric

field and electron heating, the electron temperature jumps abruptly. Figure 21 shows quantitatively how the electron temperature builds up in the considered flow model at the various inductions, B_0 . Note that $(T_e - T_0)$ increases at a rate less than proportional to B_0^2 for increasing B_0 .

The buildup of the intercomponent thermal nonequilibrium can be explained on an elementary analytical basis by considering that within $0 \leq x \leq \ell_T$ the fields—with exception of T_e —remain practically constant, and that the electron-neutral interactions predominate under the conditions given. Disregarding the strong T_e -dependence of the Coulomb interactions, ($Q_{ei} \sim T_e^{-2}$) Equation (11), taken for $s = e$, indicates a convective buildup length of the order

$$\ell_T = \frac{v_{e\parallel}}{2 \sum_{r \neq e} \frac{m_{er}}{m_r} \tau_{er}^{-1}} \quad (25)$$

Neglecting the Coulomb interaction term, one finds with the initial values and constants of Tables II and III

$$\ell_T = \frac{v_{e\parallel}}{\frac{16}{3} \sqrt{\frac{2kT_0}{\pi m_e}} \left(1 + \frac{m_0}{m_a} \frac{n_a Q_{ea}}{n_0 Q_{eo}} \right) \frac{m_e}{m_0} n_0 Q_{eo}} \cong 10^{-2} \text{ cm} \quad (26)$$

Above $x = \ell_T$, the plasma is quasi-homogeneous. Consequently, in establishing the energy balance for the electron component in the plateau region, the convective terms in Equation (11), taken for $s = e$, may be neglected. The balance gives—after eliminating in the same approximation the drift velocities by means of Equation (7)—for the plateau electron temperature ($T_{i,a} \cong T_0$)

$$\frac{T_e}{T_0} = 1 + \left(\frac{E'_\perp}{E_f} \right)^2 - \delta \quad (27)$$

where $\vec{E}'_\perp = \vec{E}_\perp + \vec{V} \times \vec{B}$ is the field producing the electron heating and E_f is the critical plasma field for electron heating,⁷

$$E_f = \frac{1}{c} \sqrt{3 m_e k T_0 \sum_{r \neq e} \tau_{er}^{-1} \sum_{r \neq e} \frac{m_{er}}{m_r} \tau_{er}^{-1}} \quad (28)$$

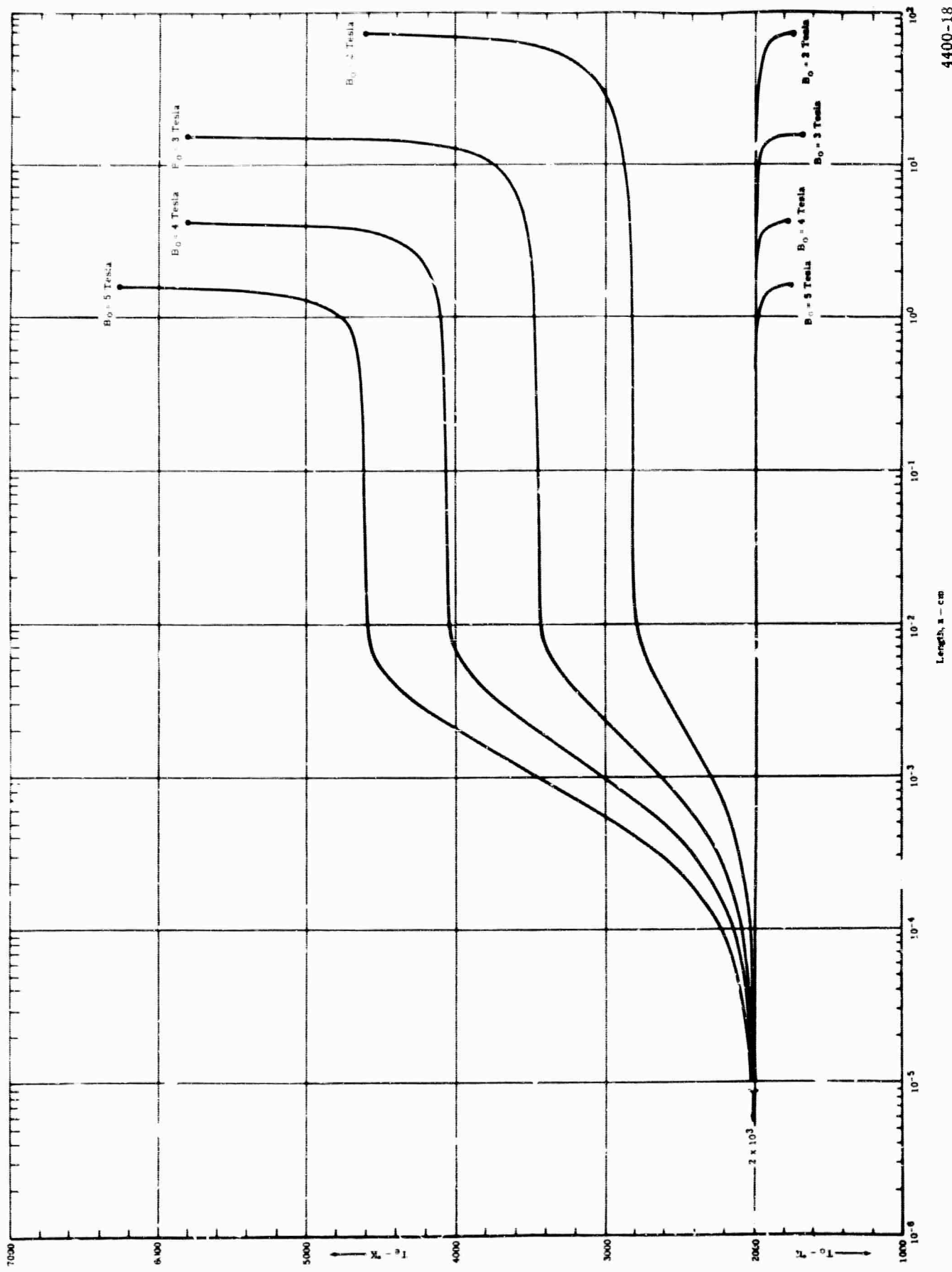


Figure 21. Intercomponent thermal nonequilibrium.

Allison

The last term, δ , is due to the inelastic energy source, and of importance in strong reactive nonequilibrium, $\Gamma^+ \neq \Gamma^-$,

$$\delta = \frac{\Gamma^+ - \Gamma^-}{3 n_e \sum_{r \neq e} \frac{m_{er}}{m_r} \tau_{er}^{-1}} \cdot \frac{\epsilon_n}{k T_0} \quad (29)$$

This equation is transcendent in T_e , and admits of no explicit analytical solution. However, neglecting the Coulomb interaction terms and the inelastic source terms, Equation (29) becomes a quadratic equation in T_e/T_0 . The latter has the solution:

$$\frac{T_e}{T_0} = \frac{1 + \sqrt{1 + 4 (E_f^0/E_f^0)^2}}{2} \quad (30)$$

where

$$E_f^0 = \frac{8}{e} \sqrt{\frac{2}{3\pi}} \frac{m_e}{m_0} \left[1 + \frac{m_0}{m_a} \frac{n_a Q_{ea}}{n_0 Q_{eo}} \right] \left[1 + \frac{n_a Q_{ea}}{n_0 Q_{eo}} \right] \cdot n_0 k T_0 \cdot Q_{eo} \quad (31)$$

The initial values and constants of Tables II and III give

$$E_f^0 = 29.31 \text{ v/cm.}$$

As an application, the plateau electron temperatures are given in Table IV according to Equation (30) for the different inductions B_0 .

Table IV.
Plateau electron temperatures.

B_0 — Tesla	2.00	3.00	4.00	5.00
$E_f^0 = V_0 B_0$ — v/cm	23.10	34.65	46.20	57.75
T_e — K	2866	3565	4309	5070

The deviations from the numerical T_e -values (1 to 10%) indicate that at extremely high inductions the effects of flow inhomogeneity and reactive nonequilibrium acquire increasing influence.

Buildup of Nonequilibrium Electron Density

To understand the ionization in a steady plasma flow, consider first a highly idealized magnetoactive plasma flow. The latter is quasi-homogeneous and may exhibit a relatively infinitely

Allison

extended electron temperature plateau, $T_e = \text{constant} > T_{e,0}$ above a negligible small length, ℓ_T . The electron density at $x = 0$ is in equilibrium with the gas temperature: $n_{e,0} = n_{e,0}(T_0)$. Further assume that the developing ionization reactions do not disturb the uniformity of the flow and that the electron density remains small compared to the atom density: $n_e \ll n_a$, i.e., $n_a \approx n_{a,0} = \text{constant}$. From Equation (3), taken for $s = e$, there follows under these conditions the "relaxation" length within which the electron density builds up due to ionization:

$$\ell_s = \frac{v_{\text{eff}}}{n_{a,0} S_{ea}(T_e)} \quad (32)$$

In Table V, ℓ_s is given based on the initial values and constants of Tables II and III, while T_e is taken in accordance with the plateau electron temperature of Figure 21.

Table V.
Relaxation lengths.

$B_0 - \text{Tesla}$	2.00	3.00	4.00	5.00
$T_e - ^\circ\text{K}$	2820	3455	4070	4615
$\ell_s - \text{cm}$	2.73×10^2	1.36×10^4	1.76×10^0	4.45×10^{-1}

In Figure 22, it is shown quantitatively how the nonequilibrium electron density, n_e , develops in the considered flow model at different inductions B_0 . As an essential result, we recognize that n_e does not increase noticeably in the T_e -plateau region. For explanation, compare the hypothetical ionization length ℓ_s , given previously, with the extension of the T_e -plateau, to be estimated from Figure 21. Throughout the T_e -plateau region, n_e does not correspond to an ionization equilibrium determined by T_e , rather in orders of magnitude $0[n_e] \approx 0[n_{e,0}]$. Under the strong nonequilibrium conditions developing at the end of the subsonic flow zone, Γ^+ and n_e increase steeply, however, even there no ionization equilibrium determined by T_e is reached. For explanation, it is remembered that the change of T_e is produced by elastic collisions and accordingly represents a relatively quick process, while the change of n_e is produced in the main by inelastic collisions and accordingly represents a relatively slow process.

An increase of the electron density would increase the magnetic force density and make the flow jump to $M \rightarrow 1$. It appears that these effects—increasing n_e and M —condition each other. This would mean that the result obtained for our special flow model—namely, that electron density increases strongly in the final region where the flow becomes sonic, has a much more general validity.

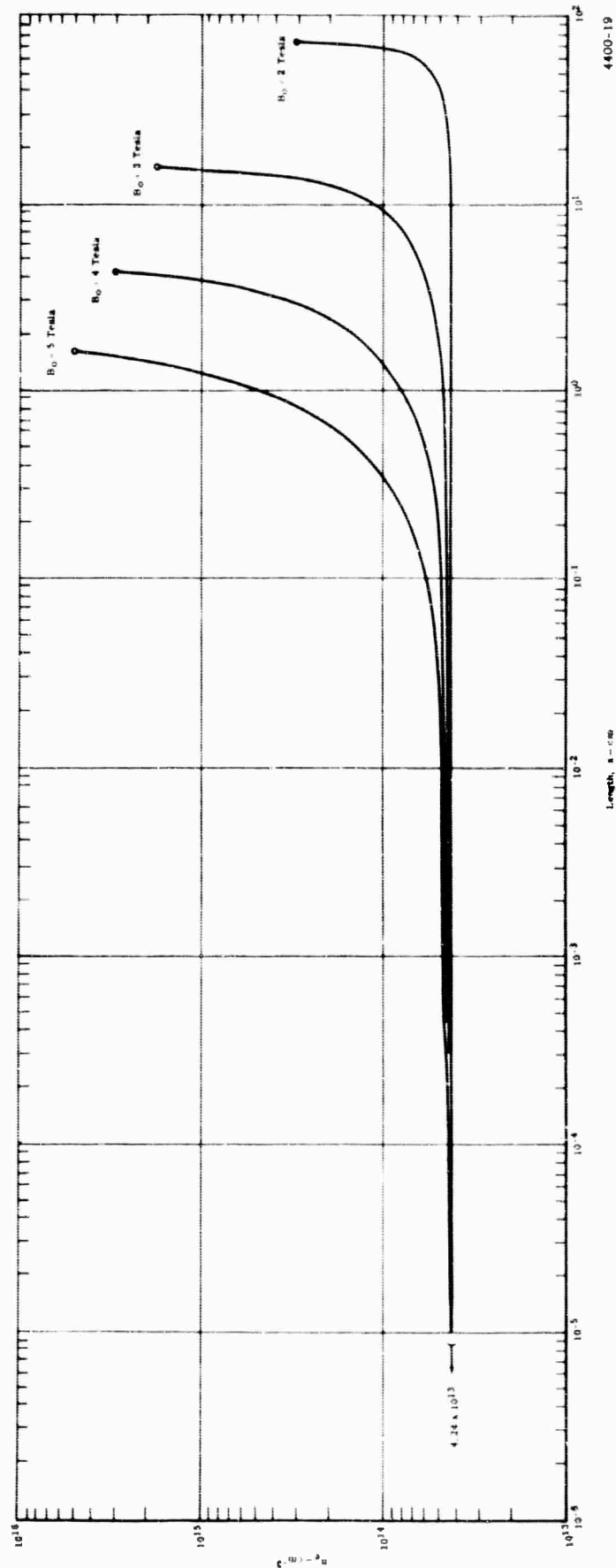


Figure 22. Buildup of electron density.

Finally, in Figure 23, it is shown quantitatively how the current density, \vec{j} , changes in the considered flow model for different inductions, B_0 . It is noteworthy that in the region of the electron temperature plateau, \vec{j} is depressed. This is due to the reduction of the electrical conductivity by the elevation of T_e at constant n_e ($\sigma \sim n_e T_e^{-1/2}$). Beyond the end of the T_e -plateau region, the electrical conductivity increases due to the stronger dependence on n_e . As the induced electric field increases in this region, j increases there also. The magnetic force density changes proportional to j , as the induced magnetic field, B_* , is small compared to the applied field, B_0 .

CONCLUSIONS

A model for a one-dimensional magnetoactive flow of a nonisothermal reacting four-component plasma has been conceived. Based on multifluid field equations, the nonequilibrium processes developing in the subsonic region of the flow have been computed via numerical integration. Parallel to that, an elementary analytical theory has been established explaining the numerical results in terms of simple functional relationships.²⁶

Understanding that quantitative statements apply to the considered plasma model and initial conditions, the following conclusions can be drawn.

- The force density resulting from the interaction of the induced current density and the magnetic field, and the nonadiabatic effects cause a decrease of the static pressure and an increase of the dynamic pressure in the subsonic flow. These field changes are most pronounced close to the end of the subsonic flow region where the singularity $M=1$ is approached.
- The power liberated by the friction of the interpenetrating components causes the flow to become nonisothermal, the nonisothermy being quantitatively important between the electron gas and the remaining plasma. After a buildup length of $\ell_T = 10^{-2}$ cm, the electron component exhibits an elevated, nearly constant temperature (T_e -plateau) extending up to that point beyond which the Mach number increases strongly towards $M=1$.
- The electron density does not change its order of magnitude (compared to its initial value) throughout the T_e -plateau region, even at extreme high B_0 -fields. The flow exhibits a strong reactive nonequilibrium in which the electron density does not correspond to its equilibrium value with the electron temperature. The assumption of an ionization equilibrium in that region made frequently in the literature must be rejected.
- Close to the end of the subsonic flow region the Mach number increases steeply towards the singularity $M=1$, where the nonequilibrium conditions become extremely strong. Electron temperature, ionization reaction velocity, and electron density practically jump in this region. There the electron density changes its order of magnitude. Recombination processes are unessential in the whole subsonic flow region (n_e is always below its equilibrium value with $T_{e'}$).

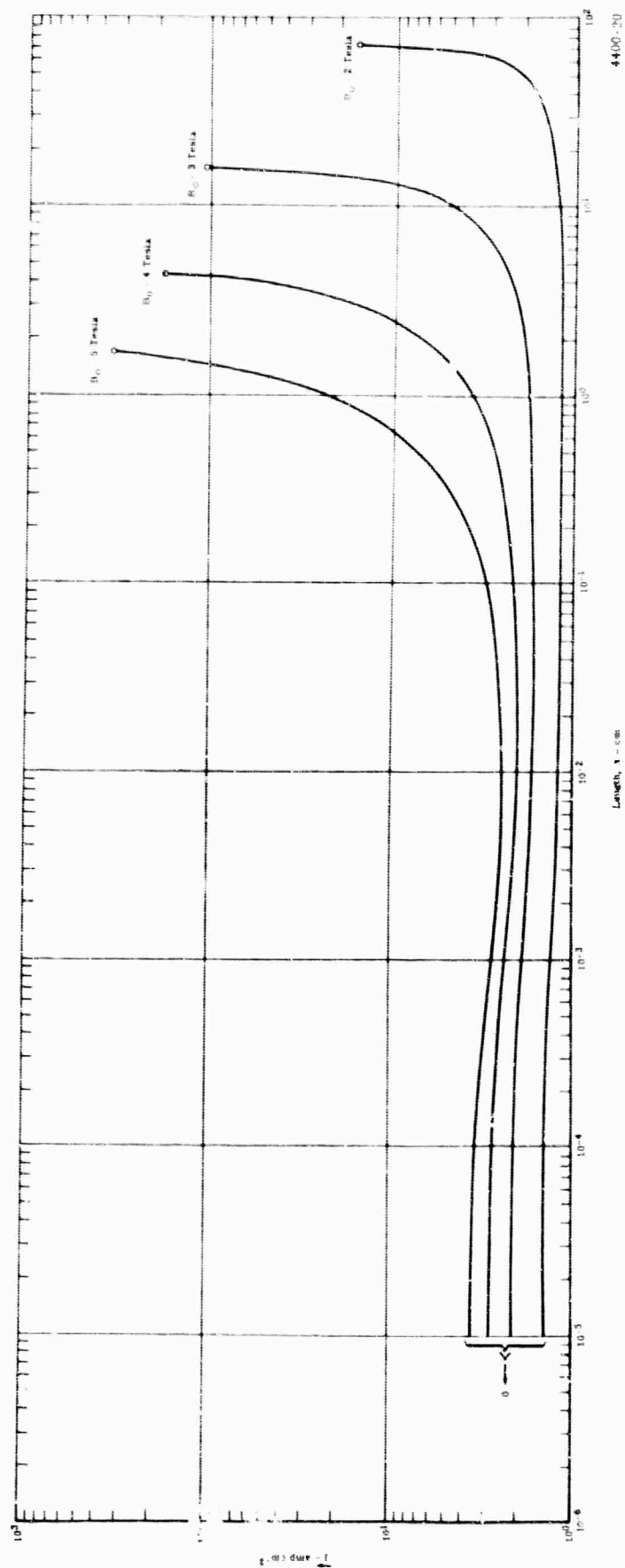


Figure 23. Buildup of current density.

Allison

The calculations have been carried through in a dissipative approximation considering inter-component friction. Consequently, the extremely strong nonequilibrium effects obtained close to the end of the subsonic flow ($M \rightarrow 1$) must be interpreted more qualitatively than quantitatively. Due to the strong inhomogeneity of the flow in this final region, viscous dissipation ($\sim v^2 v_s$) and thermal conductive dissipation ($\sim \nabla^2 T_s$) acquire increasing influence, and have to be taken into account in a more refined theory.

Allison

VII. CONCLUSIONS

During the report period, a closed loop MPD power generation device was designed, constructed, and operated. Two modes of operation were observed—saturating and nonsaturating. The saturating mode is associated with low seeding ratios while the nonsaturating mode is associated with high seeding ratios and high leakage resistances. During operation, leakage resistances varied between 0.1 and 1.0 megohms.

Of the two modes observed, only the saturating mode was investigated thoroughly. The observations were made under the following conditions:

- Pressure—slightly above atmospheric
- Magnetic field—up to 21,500 gauss
- Velocities—up to 250 m/sec at the channel entrance
- Temperatures (static)—up to 1500°K

For the saturating mode at these conditions, no nonequilibrium ionization was observed.

Theoretical considerations, as discussed in Section VI, indicate that to observe nonequilibrium ionization, runs should be made at lower pressures and higher velocities and temperatures than those stated previously. Such runs are planned during the remainder of the program.

BLANK PAGE

Allison

VIII. REFERENCES

1. Quarterly Technical Summary Reports No. 1 through 8 on Contract No. Nonr-4104, Allison Division, GMC: No. 1, EDR 3511 (20 August 1963); No. 2, EDR 3632 (21 November 1963); No. 3, EDR 3743 (18 February 1964); No. 4, EDR 3861 (19 May 1964); No. 5, EDR 3965 (17 August 1964); No. 6, EDR 4037 (17 November 1964); No. 7, EDR 4124 (25 February 1965); No. 8, EDR 4296-A (25 May 1965).
2. Lindley, B. C. Research Programme on Magnetoplasmadynamic Power Generation, Contracts N62558-3127 and N62558-4180. International Research and Development Co., Ltd., Newcastle, England.
3. Talaat, M. E. Research Program on Closed Cycle Magnetoplasmadynamic Electrical Power Generation with Nonequilibrium Ionization. Contract No. Nonr-3866(00). Martin Marietta Corporation, Baltimore, Md.
4. Hundstad, R. L. Long Life Closed Loop MHD Research and Development Unit. Contract No. AF33(657)-8311. Westinghouse Electric Corporation, Pittsburgh, Pa.
5. Halsted, R. E., and Nier, A. O. "Gas Flow through the Mass Spectrometer Viscous Leak." Review of Scientific Instruments, Vol 21, No. 12 (December 1950), pp. 1019-21.
6. Druyvestein, M. J. in Physica 10, 61 (1930).
7. Ginzburg, V. L. and Gurevic, A. V. in Fortschr. Physik 8, 97 (1960).
8. Schlueter, A. in Z. Naturforsch 6a, 73 (1951).
9. Fetz, H. in Ann. Physik 40, 595 (1943).
10. Cobine, J. D. Gaseous Conductors. New York, Dover Publications, Inc., 1958.
11. Biberman, L. M., Toropkin, Yu. N., and Ul'yanov, K. N. in Sov. Physics Techn. Physics, 7, 605 (1963).
12. Loeb, L. B. Basic Processes of Gaseous Electronics. University of California Press, 1955.
13. Elwert, G. in Z. Naturforsch. 7a, 432 (1952).

Allison

14. DeGroot, S. R. Thermodynamics of Irreversible Processes. New York, Interscience Publishers, Inc., 1951.
15. Unsöld, A. Physik der Sternatmosphären. Berlin, Springer, 1955.
16. Prigogine, I. and Mahieu, M. in Physica 16, 51 (1950).
17. Everett, W. L. in Proc. III International Symposium on Rarefied Gases, Paris, 1962.
18. Spitzer, L., Jr. Physics of Fully Ionized Gases. New York, Interscience Publishers, Inc., 1956.
19. Chapman, S. and Cowling, T. G. The Mathematical Theory of Non-Uniform Gases. Cambridge, 1958.
20. Cowling, T. G. Magnetohydrodynamics, New York, Interscience Publishers, Inc., 1957.
21. Sutton, G. W. G. E. Report R62SD990 (1962).
22. Sutton, G. W., Hurwitz, H., Poritzky, H. in Trans. AIEE, 1, 80, 687 (January 1962).
23. Wilhelm, H. E. Allison Division, General Motors Corp., EDR No. 4037, 1964 (AD608-638).
24. Knoll, M., Ollendorff, F., and Rompe, R. Gasentladungstabellen. Berlin, Springer, 1935.
25. Brown, S. C. Basic Data of Plasma Physics. New York, John Wiley & Sons, 1959.
26. Wilhelm, H. E. and Schneider, R. T. in Proceedings of the International Symposium on MHD Electrical Power Generation, Paris, 1964.